RESEARCH ARTICLE

WILEY

The Schwarz alternating method for transient solid dynamics

Alejandro Mota[1] | Irina Tezaur[2] | Gregory Phlipot[3]

[1]Mechanics of Materials, Sandia National Laboratories, Livermore, California, USA

[2]Quantitative Modeling and Analysis, Sandia National Laboratories, Livermore, California, USA

[3]Applied Physics Laboratory, John Hopkins University, Laurel, Maryland, USA

Correspondence
Alejandro Mota, Mechanics of Materials, Sandia National Laboratories, Livermore, CA 94550, USA.
Email: amota@sandia.gov

Abstract

In our earlier work, we formulated the Schwarz alternating method as a means for concurrent multiscale coupling in finite deformation solid mechanics for quasi-static problems. Herein, we advance this method for the study of transient dynamic multiscale solid mechanics problems where information is exchanged back and forth between small and large scales. The extension to dynamics relies on the notion of a global time stepper. Within each global time step, the subdomains are coupled by the standard Schwarz iterative process. Remarkably, each subdomain can use its own time step or even its own time integrator to advance its solution in time, provided that they synchronize at each global time step. We study the performance of the Schwarz method on several examples designed for this purpose. Our numerical experiments demonstrate that the method is capable of coupling regions with different mesh resolutions, different element types, and different time integration schemes (e.g., implicit and explicit), all without introducing any artifacts that afflict other coupling methods for transient dynamics. Finally, we apply the dynamic Schwarz alternating method to the simulation of a bolted joint subjected to dynamic loading, as a demonstration of the performance of the method in a realistic scenario.

KEYWORDS

concurrent multiscale coupling, finite deformation, Schwarz alternating method, transient dynamics, variational methods

1 | INTRODUCTION

An important aspect of computational simulation of mechanical systems, whether engineered or natural, is the understanding of the conditions that may lead to their failure when they are subjected to normal or abnormal environments. The failure may be the result of phenomena that develops and evolves at small scales, such as strain localization or fracture. It is not feasible, however, to conduct micro-scale simulations for macroscopic problems to fully resolve small-scale failure phenomena. So that computational resources can be efficiently allocated, it is advantageous to perform multiscale analyses. A fine scale model is used in regions to resolve fields that lead to failure phenomena. Away from these regions, a less expensive coarse scale model is used to capture the far-field behavior.[1-5]

We described in previous work a broad categorization of multiscale methods in three types, namely: sub-grid methods, homogenization methods, and concurrent methods.[6] We emphasized the ability of concurrent coupling methods to

effectively allocate computational resources to sub-domains, depending upon the need to characterize their fine-scale behavior. We also demonstrated the ability of the Schwarz alternating method for concurrent coupling between continuum-based micro-scale and macro-scale finite element simulations for the fully inelastic finite deformation problem in quasi-static scenarios. Herein, we propose an extension of the Schwarz coupling method originally developed for quasi-static finite deformation solid mechanics,[6] to the case of dynamic finite deformation solid mechanics. In particular, we seek to develop a method that lacks the reflection and refraction artifacts that have been observed with other coupling methods in dynamics.[2]

1.1 | Previous work

We described in our previous work the differences between the Schwarz alternating method for quasi-static coupling and other coupling methods.[6] In this work we concentrate on dynamic coupling.

The paramount problem in dynamic coupling is the avoidance of artifacts introduced by the coupling method itself, such as spurious reflection and refraction when waves traverse from one subdomain to another. To that end, it has been shown that coupling methods that introduce or require an overlap region between different subdomains reduce significantly the presence of these dynamic artifacts.[7]

The Schwarz alternating method was first introduced in an 1870 paper by Hermann Schwarz,[8] who used the algorithm to prove the existence of harmonic functions in irregular domains by expressing them as the union of simpler domains. The method gained prevalence in the second half of the twentieth century within the linear solver community, where it is typically used as a preconditioner for Krylov iterative methods for solving linear algebraic equations;[9-12] for a detailed overview of the Schwarz alternating method as a linear solver/preconditioner, the reader is referred to Gander[13] and the references therein. Although it is somewhat natural to formulate the method as a discretization method for multiscale partial differential equations (PDEs), surprisingly few works employ the method in this way. In recent years, several authors have used the method for concurrent multiscale coupling of atomistic and continuum scales statically, for example, Hadjiconstantinou and Patera,[14] Parks et al.,[5] and Pandurangan et al.,[15] as well as dynamically, for example, Werder et al.[16] In these works, different numerical schemes are applied in the atomistic and continuum regions, each restricted to its own subdomain, and the transfer of information from the continuum to the atomistic scale occurs in the overlap region. A domain decomposition and multiplicative alternating Schwarz-type procedure is developed for coupled atomistic/dislocation dynamics (CADD) simulations in the series of papers by Anciaux et al.,[17] Hodapp et al.,[18] Cho et al.[19] This method iterates quasistatically between the atomistic and dislocation dynamics subproblems following a domain decomposition into the atomistic and continuum domain. The dislocation line is detected automatically by the algorithm. Schwarz-like methods have also been proposed to couple dynamically distinct physics in different subdomains, for example, fluid-structure interaction,[20] and computational fluid dynamics with aero-acoustics.[21,22] Recent years have additionally seen the development of Schwarz-like methods for coupling conventional and data-driven models, including proper orthogonal decomposition (POD) reduced order models (ROMs)[23-25] as well as physics-informed neural networks (PINNs).[26,27] The majority of this work has focused on flow problems and steady elliptic equations, and the resulting hybrid methods are not always constructed for the purpose of multiscale coupling; for example, the main objective of the deep domain decomposition (D3M) approach proposed by Li et al.[26] is to reduce the risk of over-fitting when constructing a PINN. Our recent work[6] was the first to our knowledge to propose the use of the Schwarz alternating method to accomplish concurrent multiscale continuum-to-continuum coupling for finite-deformation solid mechanics. In this earlier work, attention was focused on quasi-static solid mechanics. Methods such as global-local coupling are closely related to mortar methods in that they introduce Lagrange mutipliers that require careful selection of function spaces for the formulation to be stable.[28,29] There are also global-local dynamic methods but these are not concurrent.[30] We argue that concurrency is necessary for the effective modeling of failure phenomena such as strain localization.[6] There are also methods that improve upon the convergence rate of the Schwarz method, but they require approximations that yield governing equations that use linear differential operators only.[31]

The aim of the present work is to extend our earlier Schwarz formulation to the case of dynamics. We emphasize that our Schwarz framework is fundamentally different from traditional Schwarz alternating methods, which utilize the Schwarz alternating method as a preconditioner to speed up the convergence of Krylov iterative methods for solving linear algebraic equations. In contrast, the present work develops the method as a nonlinear solver and discretization method for solving multiscale dynamic problems in solid mechanics. This extension uses a governing time stepping algorithm that controls time integrators within each domain (Figure 1), which allows the
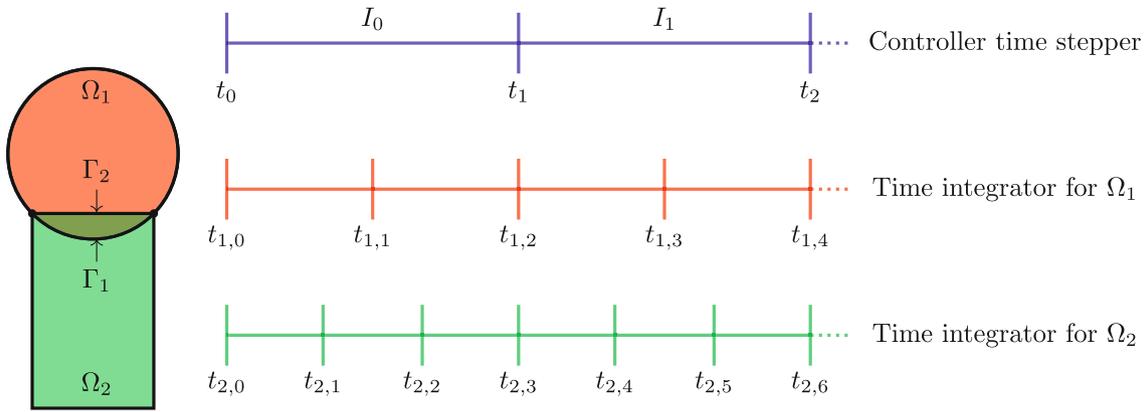
FIGURE 1 Two subdomains Ω_1 and Ω_2 and the corresponding boundaries Γ_1 and Γ_2. The blue global controller stepper has global time stops $t_0 < t_1 < \cdots < t_N$. They are convenient markers for events of interest, and for synchronization of the Schwarz algorithm. They also define the periods or intervals in which the solutions of the initial boundary value problem (8), corresponding to the action functional (4), are determined by means of the Schwarz alternating method
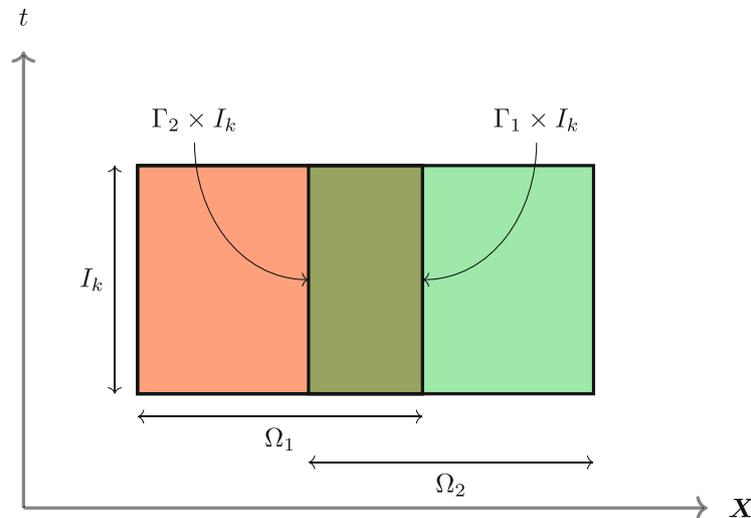
FIGURE 2 Two subdomains Ω_1 and Ω_2 and the time interval $I_k := \{t \in [t_k, t_{k+1}]\}$. The Schwarz Algorithm 1 may be interpreted as applying the traditional Schwarz alternating iterations in spacetime between $\Omega_1 \times I_k$ and $\Omega_2 \times I_k$. In this view, the Schwarz boundaries are $\Gamma_1 \times I_k$ and $\Gamma_2 \times I_k$, respectively

usage of different integrators (e.g., implicit, explicit) with different time steps in each domain. We note that the dynamic Schwarz formulation can be viewed as acting in the space-time domain, as depicted in Figure 2, similar to the formulation described in section 11.6.1 of Mathew[11] for parabolic equations. We emphasize, however, that a space-time framework/code is not required to implement the method. The approach is also fundamentally different from Schwarz waveform relaxation algorithms,[32] iterative domain-decomposition-based methods for accelerating the time-advancement of hyperbolic and parabolic problems that can work with time-parallel methods such as the parallel algorithm.

1.2 | Convergence and theoretical properties

While a number of authors have studied the convergence of the Schwarz alternating method, including Hermann Schwarz himself, most of these analyses are restricted to the application of the method to elliptic problems. The original proof by Schwarz considered linear elliptic second order equations and utilized the maximum principle.[8] Subsequent

authors employed variational methods, which were considered by Sobolev[33] for linear elasticity, and by Mikhlin[34] and Prager[35] for polyharmonic functions. Higher-order linear equations, for example, biharmonic, were studied by Morgenstern[36] and Babuška,[37] among others. Many of these works applied variational ideas after recasting the method as a series of successive projections. The application of Schwarz to nonlinear equations was not considered until the 1980s, when a series of authors, including Lions,[38] Badea,[39] and Lui[40] proved convergence of the method for certain types of nonlinear monotone problems. In Mota et al.[6] we proved that the Schwarz alternating method converges for the finite-deformation solid mechanics problem under the conditions that the single-domain problem is well-posed and that the overlap region is non-empty, a critical requirement for convergence.[9-12] In the case of coupling with no overlap with Dirichlet boundary conditions, the theory says that the method will fail to converge. There are variants of the Schwarz method that do not require overlap, but they need other types of boundary conditions, such as Dirichlet-Neumann or Robin-Robin. We explore a subset of such variants elsewhere in the context of contact mechanics.[41] Although greater amounts of overlap improve the rate of convergence, this requires redundant computation in the overlap region. Thus, it is often the case that meshes or CAD designs are used as is for Schwarz coupling as long as there is some amount of overlap.

The majority of the references enumerated above consider elliptic problems, specifically problems that are independent of time. Very little work has been done on the analysis of the Schwarz alternating method in the context of time-dependent, parabolic or hyperbolic PDEs. Lions[38] sketched out several possible dynamic Schwarz formulations for parabolic and hyperbolic problems, namely the transient heat equation and the wave equation, respectively. A proof of *a priori* convergence of several of these dynamic Schwarz algorithms is outlined. Convergence analysis of a dynamic Schwarz algorithm is performed by Boglaev et al.[42] in the context of transient 2D eddy-current problem, a parabolic PDE that can be considered a "singularly perturbed" problem whose solution exhibits boundary layers. Two Schwarz-like algorithms that combine a domain-decomposition-based handling of the spatial problem together with a time-discretization scheme are presented. Convergence is proven and an algebraic convergence rate is established.

For the finite deformation solid dynamics problem, it proves convenient to formulate the problem in terms of the Variational Principle of Hamilton. We discuss the conditions under which the corresponding action functional is strictly convex or strictly concave. In these cases, the convergence analysis follows directly from our previous work for the quasi-static case.[6] For all other cases, it is necessary to introduce discretizations in space and time to probe further the nature of the action functional. We develop a heuristic test to determine whether the discrete action functional is convex, and therefore whether the Schwarz algorithm will converge.

1.3 | Scope and organization

The remainder of this article is organized as follows. The Schwarz alternating method for dynamic finite deformation solid mechanics problem is presented in variational form in Section 2. Section 3 is devoted to numerical experiments on which we study the accuracy and performance of the proposed method. We describe succinctly our implementation of the method within two finite element codes known as ALBANY LCM and SIERRA (Section 3.1). In Section 3.2, we discuss some of the convergence and error analyses in our subsequent numerical studies. Following these preliminaries, three dynamic mechanics problem are considered in the order of increasing complexity: a linear elastic wave propagation problem on a clamped bar geometry (Section 3.3), a problem involving a nonlinear elastic bar subjected to a high degree of torsion (Section 3.4), and a problem involving a realistic inelastic bolted joint specimen (Section 3.5). The former two simulations are performed using the ALBANY LCM code base, whereas the latter is performed using SIERRA. Results are discussed and conclusions are drawn in Section 4. Some remarks about the conditions necessary for the convergence of the Schwarz alternating method for finite deformation solid dynamics are made in Appendix A.

2 | FORMULATION OF THE SCHWARZ ALTERNATING METHOD FOR TRANSIENT SOLID DYNAMICS

We start by defining the standard finite deformation variational formulation to establish notation before presenting the formulation of the coupling method.

2.1 | Variational formulation on a single domain

Let $I := \{t \in [t_0, t_1]\}$ be a closed time interval with $0 \le t_0 < t_1$, and $t_0, t_1 \in \mathbb{R}$, and consider a body as the regular open set $\Omega \subset \mathbb{R}^3$ undergoing a motion described by the mapping $\boldsymbol{x} = \boldsymbol{\varphi}(\boldsymbol{X}, t) : \Omega \times I \to \mathbb{R}^3$, where $\boldsymbol{X} \in \Omega$ and $t \in I$. Assume that the boundary of the body is $\partial\Omega = \partial_\varphi\Omega \cup \partial_T\Omega$ with unit normal $\boldsymbol{N}$, where $\partial_\varphi\Omega$ is a prescribed position boundary, $\partial_T\Omega$ is a prescribed traction boundary, and $\partial_\varphi\Omega \cap \partial_T\Omega = \emptyset$. The prescribed boundary positions or Dirichlet boundary conditions are $\boldsymbol{\chi} : \partial_\varphi\Omega \times I \to \mathbb{R}^3$. The prescribed boundary tractions or Neumann boundary conditions are $\boldsymbol{T} : \partial_T\Omega \times I \to \mathbb{R}^3$. Let $\boldsymbol{F} := \mathrm{Grad}\ \boldsymbol{\varphi}$ be the deformation gradient. Let the initial position and velocity at time t_0 be $\boldsymbol{x}_0 \equiv \boldsymbol{X} : \Omega \to \mathbb{R}^3$, and $\boldsymbol{v}_0 : \Omega \to \mathbb{R}^3$, correspondingly. Let also $\rho_0 \boldsymbol{B} : \Omega \to \mathbb{R}^3$ be the body force, with ρ_0 the mass density in the reference configuration. Furthermore, introduce the kinetic energy of the body as

$$T(\dot{\boldsymbol{\varphi}}) := \frac{1}{2} \int_\Omega \rho_0 \dot{\boldsymbol{\varphi}} \cdot \dot{\boldsymbol{\varphi}}\ \mathrm{d}V, \tag{1}$$

and its potential energy as

$$V(\boldsymbol{\varphi}) := \int_\Omega A(\boldsymbol{F}, \boldsymbol{Z})\ \mathrm{d}V - \int_\Omega \rho_0 \boldsymbol{B} \cdot \boldsymbol{\varphi}\ \mathrm{d}V - \int_{\partial_T\Omega} \boldsymbol{T} \cdot \boldsymbol{\varphi}\ \mathrm{d}S, \tag{2}$$

in which $A(\boldsymbol{F}, \boldsymbol{Z})$ is the Helmholtz free-energy density and $\boldsymbol{Z}$ is a collection of internal variables. The Lagrangian function of the body is then

$$L(\boldsymbol{\varphi}, \dot{\boldsymbol{\varphi}}) := T(\dot{\boldsymbol{\varphi}}) - V(\boldsymbol{\varphi}), \tag{3}$$

which gives rise to the action functional

$$S[\boldsymbol{\varphi}] := \int_I L(\boldsymbol{\varphi}, \dot{\boldsymbol{\varphi}})\ \mathrm{d}t. \tag{4}$$

According to the Variational Principle of Hamilton, the equation of motion is obtained by finding the critical point of the action functional $S[\boldsymbol{\varphi}]$ over the Sobolev space $W_2^1(\Omega \times I)$ that is comprised of all functions that are square-integrable and have square-integrable first derivatives, for fixed endpoints of the deformation mapping at t_0 and t_1.[43] Define

$$S := \left\{ \boldsymbol{\varphi} \in W_2^1(\Omega \times I) : \boldsymbol{\varphi} = \boldsymbol{\chi}\ \mathrm{on}\ \partial_\varphi\Omega \times I; \boldsymbol{\varphi} = \boldsymbol{x}_0\ \mathrm{on}\ \Omega \times t_0; \boldsymbol{\varphi} = \boldsymbol{x}_1\ \mathrm{on}\ \Omega \times t_1 \right\}, \tag{5}$$

and

$$\mathcal{V} := \left\{ \boldsymbol{\xi} \in W_2^1(\Omega \times I) : \boldsymbol{\xi} = \boldsymbol{0}\ \mathrm{on}\ \partial_\varphi\Omega \times I \cup \Omega \times t_0 \cup \Omega \times t_1 \right\}, \tag{6}$$

where $\boldsymbol{\xi}$ is a test function. This leads to

$$\begin{aligned} \delta S := DS[\boldsymbol{\varphi}](\boldsymbol{\xi}) &= \int_I \left(\frac{\partial L}{\partial \boldsymbol{\varphi}} \cdot \boldsymbol{\xi} + \frac{\partial L}{\partial \dot{\boldsymbol{\varphi}}} \cdot \dot{\boldsymbol{\xi}} \right)\ \mathrm{d}t = \int_I \left(\frac{\partial L}{\partial \boldsymbol{\varphi}} - \frac{\mathrm{d}}{\mathrm{d}t} \frac{\partial L}{\partial \dot{\boldsymbol{\varphi}}} \right) \cdot \boldsymbol{\xi}\ \mathrm{d}t \\ &= \int_I \left[\int_\Omega \left(\rho_0 \boldsymbol{B} \cdot \boldsymbol{\xi} - \boldsymbol{P} : \mathrm{Grad}\ \boldsymbol{\xi} + \rho_0 \dot{\boldsymbol{\varphi}} \cdot \dot{\boldsymbol{\xi}} \right)\ \mathrm{d}V + \int_{\partial_T\Omega} \boldsymbol{T} \cdot \boldsymbol{\xi}\ \mathrm{d}S \right]\ \mathrm{d}t \\ &= \int_I \left[\int_\Omega (\mathrm{Div}\ \boldsymbol{P} + \rho_0 \boldsymbol{B} - \rho_0 \ddot{\boldsymbol{\varphi}}) \cdot \boldsymbol{\xi}\ \mathrm{d}V + \int_{\partial_T\Omega} \boldsymbol{T} \cdot \boldsymbol{\xi}\ \mathrm{d}S \right]\ \mathrm{d}t = 0, \end{aligned} \tag{7}$$

where $\boldsymbol{P} = \partial A / \partial \boldsymbol{F}$ denotes the first Piola–Kirchhoff stress. The Euler–Lagrange equation corresponding to (4) is then

$$\mathrm{Div}\ \boldsymbol{P} + \rho_0 \boldsymbol{B} = \rho_0 \ddot{\boldsymbol{\varphi}} \quad \mathrm{in} \quad \Omega \times I, \tag{8}$$

with initial conditions

$$\varphi(\mathbf{X}, t_0) = \mathbf{x}_0 \quad \text{in} \quad \Omega,$$
$$\dot{\varphi}(\mathbf{X}, t_0) = \mathbf{v}_0 \quad \text{in} \quad \Omega, \tag{9}$$

and boundary conditions

$$\varphi(\mathbf{X}, t) = \chi \quad \text{on} \quad \partial_\varphi \Omega \times I,$$
$$\mathbf{PN} = \mathbf{T} \quad \text{on} \quad \partial_T \Omega \times I. \tag{10}$$

2.2 | Coupling two or more subdomains via the Schwarz alternating method for transient solid dynamics

In this section, we describe a variant of the Schwarz alternating method for coupling multiple overlapping subdomains for transient solid dynamics. Consider without loss of generality a partition of the domain Ω into two open subsets or subdomains Ω_1 and Ω_2, such that $\Omega = \Omega_1 \cup \Omega_2$ and $\Omega_1 \cap \Omega_2 \neq \emptyset$ as shown in Figure 1. Consider also the existence of a global controller stepper that defines global time stops $t_0 < t_1 < \cdots < t_N \in \mathbb{R}$, with $N \in \mathbb{N}$ denoting a pre-defined number of global time steps. The global time steps may be equal or not. They serve the purpose of convenient markers in time for events of interest, and for synchronization of the Schwarz algorithm. Crucially, they also define the periods or intervals in which the solutions of the initial boundary value problem (8), corresponding to the action functional (4), are determined by means of the Schwarz alternating method.

In keeping with other works on the convergence of the Schwarz alternating method, we introduce a set of indices that alternate between the subdomains as

$$n \in \mathbb{N}^0 = \{0, 1, 2, \dots\}, \quad i = 2 - n + 2 \left\lfloor \frac{n}{2} \right\rfloor \in \{1, 2\}, \quad j = n + 1 - 2 \left\lfloor \frac{n}{2} \right\rfloor \in \{1, 2\}, \tag{11}$$

that is $i = 1$ and $j = 2$ if n is odd, and $i = 2$ and $j = 1$ if n is even. Introduce the following definitions for each subdomain i:

- Closure: $\overline{\Omega}_i := \Omega_i \cup \partial \Omega_i$.
- Dirichlet boundary: $\partial_\varphi \Omega_i := \partial_\varphi \Omega \cap \overline{\Omega}_i$.
- Neumann boundary: $\partial_T \Omega_i := \partial_T \Omega \cap \overline{\Omega}_i$.
- Schwarz boundary: $\Gamma_i := \partial \Omega_i \cap \Omega_j$.

Note that with these definitions we guarantee that $\partial_\varphi \Omega_i \cap \partial_T \Omega_i = \emptyset$, $\partial_\varphi \Omega_i \cap \Gamma_i = \emptyset$ and $\partial_T \Omega_i \cap \Gamma_i = \emptyset$. Let us also introduce the closed time interval $I_k := \{t \in [t_k, t_{k+1}]\}$, with $k \in \{0, \dots, N-1\}$. Now define the spaces

$$S_i := \left\{ \varphi \in W_2^1(\Omega_i \times I_k) : \varphi = \chi \quad \text{on} \quad \partial_\varphi \Omega_i \times I_k, \right.$$
$$\varphi = P_{\Omega_j \to \Gamma_i}[\varphi(\Omega_j, I_k)] \quad \text{on} \quad \Gamma_i \times I_k,$$
$$\left. \varphi = \mathbf{x}_k^{(i)} \quad \text{on} \quad \Omega_i \times t_k \right\}, \tag{12}$$

and

$$\mathcal{V}_i := \{\xi \in W_2^1(\Omega_i \times I_k) : \xi = \mathbf{0} \quad \text{on} \quad [(\partial_\varphi \Omega_i \cup \Gamma_i) \times I_k] \cup (\Omega_i \times t_k)\}, \tag{13}$$

where $\mathbf{x}_k^{(i)}$ is the known position at time t_k for subdomain Ω_i, and the symbol $P_{\Omega_j \to \Gamma_i}[\cdot]$ denotes the projection from the subdomain Ω_j onto the Schwarz boundary Γ_i. This projection operator plays a central role in the Schwarz alternating method. For the moment it is sufficient to assume that the operator is able to project a field φ from one subdomain to the Schwarz boundary of the other subdomain. The action functional for subdomain Ω_i is

$$S_i[\varphi] := \int_{I_k} L_i(\varphi, \dot{\varphi}) \, dt, \tag{14}$$

with its Lagrangian function

$$L_i(\boldsymbol{\varphi}, \dot{\boldsymbol{\varphi}}) := T_i(\dot{\boldsymbol{\varphi}}) - V_i(\boldsymbol{\varphi}), \tag{15}$$

in which the kinetic energy is

$$T_i(\dot{\boldsymbol{\varphi}}) := \frac{1}{2} \int_{\Omega_i} \rho_0 \dot{\boldsymbol{\varphi}} \cdot \dot{\boldsymbol{\varphi}} \, \mathrm{d}V, \tag{16}$$

and the corresponding potential energy is

$$V_i(\boldsymbol{\varphi}) := \int_{\Omega_i} A(\boldsymbol{F}, \boldsymbol{Z}) \, \mathrm{d}V - \int_{\Omega_i} \rho_0 \boldsymbol{B} \cdot \boldsymbol{\varphi} \, \mathrm{d}V - \int_{\partial_T \Omega_i} \boldsymbol{T} \cdot \boldsymbol{\varphi} \, \mathrm{d}S. \tag{17}$$

The optimization of the functional (14) leads to a variational formulation of the form (7) and (8) for each subdomain as

$$\delta S_i := DS_i[\boldsymbol{\varphi}^{(n)}](\boldsymbol{\xi}^{(i)}) = \int_{I_k} \left(\frac{\partial L_i}{\partial \boldsymbol{\varphi}^{(n)}} \cdot \boldsymbol{\xi}^{(i)} + \frac{\partial L_i}{\partial \dot{\boldsymbol{\varphi}}^{(n)}} \cdot \dot{\boldsymbol{\xi}}^{(i)} \right) \, \mathrm{d}t$$

$$= \int_{I_k} \left(\frac{\partial L_i}{\partial \boldsymbol{\varphi}^{(n)}} - \frac{\mathrm{d}}{\mathrm{d}t} \frac{\partial L_i}{\partial \dot{\boldsymbol{\varphi}}^{(n)}} \right) \cdot \boldsymbol{\xi}^{(i)} \, \mathrm{d}t = 0, \tag{18}$$

in which $\boldsymbol{\xi}^{(i)} \in \mathcal{V}_i$. The corresponding Euler–Lagrange equations are

$$\mathrm{Div} \, \boldsymbol{P}^{(n)} + \rho_0 \boldsymbol{B} = \rho_0 \ddot{\boldsymbol{\varphi}}^{(n)} \quad \mathrm{in} \quad \Omega_i \times I_k, \tag{19}$$

with initial conditions

$$\boldsymbol{\varphi}^{(n)}(\boldsymbol{X}, t_k) = \boldsymbol{x}_k^{(i)} \quad \mathrm{in} \quad \Omega_i,$$
$$\dot{\boldsymbol{\varphi}}^{(n)}(\boldsymbol{X}, t_k) = \boldsymbol{v}_k^{(i)} \quad \mathrm{in} \quad \Omega_i, \tag{20}$$

where $\boldsymbol{\varphi}^{(n)}$ is the solution for the nth problem, and $\boldsymbol{v}_k^{(i)}$ is the known velocity at time t_k for subdomain Ω_i. We also have the following Dirichlet boundary conditions

$$\boldsymbol{\varphi}^{(n)}(\boldsymbol{X}, t) = \begin{cases} \chi, & \text{for } n \geq 0 \text{ on } \partial_{\varphi} \Omega_i \times I_k, \\ \mathrm{id}_{\boldsymbol{X}}, & \text{for } n = 0 \text{ on } \Gamma_2 \times I_k, \\ P_{\Omega_j \to \Gamma_i}[\boldsymbol{\varphi}^{(n-1)}(\Omega_j, I_k)], & \text{for } n > 0 \text{ on } \Gamma_i \times I_k, \end{cases} \tag{21}$$

where $\mathrm{id}_{\boldsymbol{X}}$ is the identity map (i.e., zero displacement, or a better guess, if available), and Neumann boundary conditions

$$\boldsymbol{PN} = \boldsymbol{T} \quad \mathrm{on} \quad \partial_T \Omega_i \times I_k. \tag{22}$$

Assume that the solutions for all subdomains Ω_i are known at time t_k. Let us further assume that those solutions constitute a partition of the global domain solution at time t_k. The Schwarz alternating method for transient solid dynamics solves a sequence of problems on Ω_1 and Ω_2 for $t \in I_k$ that converge to the solution for the entire domain Ω. The solution $\boldsymbol{\varphi}^{(n)}$ for the nth problem is obtained by solving (19) subjected to initial conditions (20) and boundary conditions (21) and (22). In summary, the dynamic Schwarz alternating method is described in Algorithm 1. While some of the individual steps in Algorithm 1 are reminiscent of the procedure used to generate the classical Schwarz preconditioner used to accelerate convergence of Krylov iterative methods, the proposed approach is fundamentally different from the majority of Schwarz-based methods in the literature, as we develop the Schwarz alternating method as a novel multiscale discretization method, rather than a linear solver.

Note that our method is indifferent to the way the subdomains are numbered. Additionally, the procedure may be extended in a straightforward way to more than two subdomains, as demonstrated for a three-subdomain weld problem

in Mota et al.[6] We emphasize that the method is indifferent to the ordering of the subdomains, that is, there is no concept or primary or secondary (or tertiary, etc.) subdomains. The Schwarz iterative process in dynamics may be interpreted as an instance of the repeated application of Hamilton's principle in each subdomain Ω_i to advance the solution of the entire domain Ω from t_k to t_{k+1} in each controller step. Within that interval, each of the Schwarz iterations finds the solution to its own dynamic problem, and this sequence of solutions converges to the solution of the entire domain. This process may also be interpreted as applying the traditional Schwarz alternating iterations in space-time between $\Omega_1 \times I_k$ and $\Omega_2 \times I_k$, as shown in Figure 2. In this view, the Schwarz boundaries are $\Gamma_1 \times I_k$ and $\Gamma_2 \times I_k$, respectively.

The solution to the action functional S_i for each subdomain is found independently from other subdomains. Within each subdomain the computation of the solution can be obtained by whatever means available, in a close analog to the quasistatic method.[6] Thus, each subdomain can advance its own solution within the interval I_k using its own time integrator, and its own time step. Crucially, there are no dynamic artifacts as the sequence of solutions derived from the Schwarz process is converging to the solution in the entire domain, which has no artifacts of its own.

As described in more detail in Section 3.1.1, the projection operator from one subdomain to another consists in the simple application of the existing finite element interpolation functions. That is, any time the value of a field is needed at a point at the boundary in one subdomain, a search is performed to determine the element containing that point in the other subdomain, and the field value is calculated by using the nodal values of that element and the corresponding interpolation functions.

Algorithm 1. Schwarz alternating method for solid transient dynamics

1: $k \leftarrow 0$
2: **repeat**   ▷ controller time stepper
3:     $\boldsymbol{\varphi}^{(0)}(\Gamma_2, I_k) \leftarrow \mathrm{id}_X$ ▷ set to zero displacement or a better guess in Γ_2
4:     $n \leftarrow 1$
5:     **repeat**   ▷ Schwarz loop
6:        $\boldsymbol{\varphi}^{(n)}(\Omega_i, t_k) \leftarrow x_k^{(i)}$ ▷ position IC
7:        $\dot{\boldsymbol{\varphi}}^{(n)}(\Omega_i, t_k) \leftarrow v_k^{(i)}$ ▷ velocity IC
8:        $\boldsymbol{\varphi}^{(n)}(\partial_\varphi \Omega_i, I_k) \leftarrow \chi$ ▷ Dirichlet BC
9:        $\boldsymbol{\varphi}^{(n)}(\Gamma_i, I_k) \leftarrow P_{\Omega_j \to \Gamma_i}[\boldsymbol{\varphi}^{(n-1)}(\Omega_j, I_k)]$ ▷ Schwarz BC
10:        $\boldsymbol{\varphi}^{(n)}(\Omega_i, I_k) \leftarrow$ solution of (19), (20), (21), (22)   ▷ solve dynamic problem on $\Omega_i \times I_k$
11:        $n \leftarrow n + 1$
12:     **until** $\epsilon^{(n)} := \left[\left(\frac{||\triangle x^{(n)}||}{||x^{(n)}||} \right)^2 + \left(\frac{||\triangle x^{(n+1)}||}{||x^{(n+1)}||} \right)^2 \right]^{1/2} \leq$ tolerance   ▷ Convergence criterion (35)
13:     $k \leftarrow k + 1$
14: **until** $k = N$ ▷ N is the total number of time steps

---

3 | NUMERICAL EXAMPLES

We have described in detail our Schwarz alternating formulation for dynamic multiscale coupling, and therefore we now present three numerical examples that demonstrate the method's convergence and properties. We employ SI units of measurement, unless otherwise indicated. The majority of the results presented herein can be reproduced by downloading and installing the ALBANY LCM code, described in Section 3.1.1. Details on how this can be done are provided in Section 4.

3.1 | Implementation

The Schwarz method for dynamic multiscale coupling described herein has been implemented within two finite-element code frameworks at Sandia National Laboratories: ALBANY LCM and SIERRA. We describe these codes succinctly below.

3.1.1 | ALBANY LCM finite element code

The ALBANY LCM framework[*] is a recently created fork of, ALBANY, an open-source[†] C++ object-oriented, parallel, unstructured-grid, implicit finite element code for solving general PDEs. ALBANY was developed using the "Agile Components" code development strategy in which mature modular libraries from the TRILINOS[44] project[‡] are glued together using template-based generic programming and abstract interfaces, giving users access to dozens of capabilities at run time simply by changing an option in the input file. Over the years, ALBANY has hosted a number of science and engineering applications, including the AERAS global atmosphere code,[45] the Albany Land-ICE (ALI)[46] ice sheet model solver, the Quantum Computer Aided Design (QCAD)[47] simulator, and the Laboratory for Computational Mechanics (LCM)[48] research code. This last project comprises ALBANY LCM and is specifically targeted at solid mechanics applications. It contains our implementation of the Schwarz alternating method described herein and in Mota et al.[6] A more detailed description of ALBANY, including a detailed description of its underlying design and the physics implemented therein, can be found in Salinger et al.[49]

A detailed discussion of several implementations of the Schwarz alternating method for coupling quasi-static problems in solid mechanics within ALBANY LCM is presented in Mota et al.[6] To enable concurrent dynamic coupling, we have implemented Algorithm 1 within ALBANY LCM. This implementation is an extension of the Schwarz variant named "Full Schwarz" in Mota et al.[6] and the reader is referred to this earlier publication for a detailed discussion of the implementation. To perform the projection of the solution from a subdomain $\Omega_i \in \mathbb{R}^3$ to a boundary of a subdomain $\Gamma_j \in \mathbb{R}^2$ for some $i, j \in \mathbb{N}$, we utilize an open-source[§] library known as Data Transfer Kit (DTK),[50] designed to provide parallel, scalable services for solution transfer between shared volumes and surfaces. For our purposes, we use DTK to perform the projection of the solution from one subdomain to another using the underlying finite element interpolation functions of the meshes of each of the subdomains. For time-stepping, our dynamic Schwarz implementation within ALBANY LCM utilizes the TEMPUS package[51] of TRILINOS, which provides a general infrastructure for the time evolution of solutions to ordinary differential equations (ODEs), PDEs, and discrete algebraic equations (DAEs), through a variety of general verified time-integration schemes.

3.1.2 | SIERRA solid mechanics code

SIERRA solid mechanics (SIERRA/SM)[52] is a Lagrangian code for the analysis of solids and structures, providing capabilities for explicit as well as implicit quasistatic and dynamic analyses. SIERRA/SM contains a versatile library of continuum and structural elements, as well as an extensive library of constitutive models. For implicit problems, SIERRA/SM uses FETI,[53] a highly scalable and efficient domain-decomposition-based parallel iterative linear solver that can be used to compute the action of the full tangent preconditioner when utilizing a nonlinear Conjugate Gradient (CG) solver. SIERRA/SM has been written for parallel computing environments, and allows for scalable solutions of very large problems for both implicit and explicit analyses.

3.2 | Error and convergence analyses

To highlight the ability of the proposed Schwarz framework to couple different element types, we employ three different types of finite elements:

1. 8-node isoparametric hexahedral elements (referred to as "hex" elements),
2. 4-node isoparametric tetrahedral elements (referred to as "tet" elements), and
3. 10-node composite tetrahedral elements (referred to as "composite tet" elements).

The composite tet elements were introduced recently,[54] where it was shown that they offer a significant improvement in terms of accuracy and computational expense over isoparametric 10-node tetrahedral elements.

We also evaluate the method's ability to couple different time integrators in different subdomains. The employed time integrators are from the Newmark-Beta family of methods,[55] which are well-suited for the dynamic solid mechanics problems of interest here. The method is defined by two parameters, $\beta, \gamma \in [0, 1]$. Here, we consider two choices for these parameters:

- $\beta = 0.25$, $\gamma = 0.5$, which yields an implicit, second-order, unconditionally stable scheme also known as the average acceleration method.
- $\beta = 0$, $\gamma = 0.5$, which yields an explicit, second-order, conditionally stable scheme, also known as the central difference method.

For the first two test cases considered, the linear elastic wave propagation problem (Section 3.3) and the torsion problem (Section 3.4), the numerical results presented below include an error analysis. For the former test case, a closed-form analytic solution is available, and relative errors are computed with respect to this solution. For general problems, an exact closed-form analytic solution is not be available. In this case, relative errors are computed with respect to a reference solution computed on a fine mesh. For such analyses, we utilize the DTK_Interp_and_Error utility built as a part of ALBANY LCM. This utility utilizes the DTK library described earlier, and operates on Exodus output files produced by both ALBANY LCM and SIERRA; for a more detailed discussion of how the utility operates, the reader is referred to Section 4.2 of Mota et al.[6] We report single time-step errors as well as time-averaged errors over multiple time-steps.

In the test cases considered, we refer to a quantity of interest known as the "overlap volume fraction." This is defined as the volume of the overlap region between a pair of Schwarz subdomains, divided by the volume of the underlying single domain geometry:

$$\text{overlap volume fraction} = \frac{\text{vol}(\Omega_i \cap \Omega_j)}{\text{vol}(\Omega)}, \tag{23}$$

for $i \neq j \in \mathbb{N}$.

3.3 | Elastic wave propagation

We begin by evaluating the application of dynamic Schwarz coupling to an elastic wave propagation problem. This problem is implemented in both ALBANY LCM as well as SIERRA, but herein we restrict attention to results obtained using the ALBANY LCM implementation. We consider a simple beam geometry of length L, and square cross section $l \times l$ that is clamped on both sides. Although the test case is one-dimensional (1D), we treat it as a three-dimensional (3D) problem within our codes. Toward this effect, $\Omega = (0, l) \times (0, l) \times (0, L) \in \mathbb{R}^3$. Here, we choose $L = 1$ m and $l = 1$ mm. Let $\boldsymbol{x} := (x, y, z)^{\mathrm{T}} \in \mathbb{R}^3$ denote the coordinate vector. To ensure 1D behavior, we set a homogeneous Dirichlet boundary condition on the x- and y-displacements at the $x = 0$, $x = l$, $y = 0$, and $y = l$ boundaries

$$u_i(x = 0, t) = u_i(x = l, t) = u_i(y = 0, t) = u_i(y = l, t) = 0, \quad i = 1, 2 \ \forall t \geq 0. \tag{24}$$

The clamped end assumption translates to a homogeneous Dirichlet boundary condition on the z-displacement at the $z = 0$ and $z = L$ boundaries

$$u_3(z = 0, t) = u_3(z = L, t) = 0, \quad \forall t \geq 0. \tag{25}$$

A simple linear elastic material model with Young's modulus $E = 1$ GPa, density $\rho = 1000$ kg/m^3 and Poisson's ratio $\nu = 0$ is prescribed. Let

$$f(z) = \frac{a}{2} \exp\left[-\frac{(z - b)^2}{2s^2}\right], \tag{26}$$

for $a, b, s \in \mathbb{R}$. The initial condition is a Gaussian of the form

$$u_3(\mathbf{x}, 0) = 2f(z), \quad \boldsymbol{x} \in \Omega, \quad z \in (0, L), \tag{27}$$

where $a = 0.01$, $b = 0.5$, $s = 0.02$. From standard wave equation analysis, the wave speed $c = \sqrt{E/\rho} = 1$ km/s. It is straightforward to show using separation of variables that the exact solution for the z-displacement is

$$u_3(\mathbf{x}, t) = f(z - ct) + f(z + ct) - f(z - c(T - t)) - f(z + c(T - t)), \tag{28}$$

which includes the two terms due to the first wave reflection at the ends, and where $T = L/c = 1$ ms. It follows that the z-velocity is

$$\dot{u}_3(\mathbf{x}, t) = \frac{c}{s^2} \{(z - ct - b)f(z - ct) - (z + ct - b)f(z + ct)$$
$$- [z - c(T - t) - b]f[z - c(T - t)] - [z + c(T - t) - b]f[z + c(T - t)]\} . \tag{29}$$

For a mesh resolution of $\triangle z = 1$ mm, the time step needed to resolve the wave is $\triangle t \leq \triangle z/c = 1\mu$s. One can see from (28) that the exact solution satisfies

$$u_3(\mathbf{x}, T) = -u_3(\mathbf{x}, 0) \quad \text{at} \quad T = L/c = 1 \text{ ms}, \tag{30}$$

that is, the solution should be the mirror image of the initial condition at $T = L/c = 1$ ms. Although deceptively simple, this problem is a very stringent test case that reveals possible coupling artifacts, for example, spurious oscillations and/or lack of energy conservation.

3.3.1 | Baseline single-domain results

Prior to evaluating our dynamic alternating Schwarz formulation on the linear elastic wave propagation problem, we provide some baseline results obtained by solving the problem using a standard finite element formulation in our ALBANY LCM code base. We discretize the domain $\Omega = (0, 0.001) \times (0, 0.001) \times (0, 1)$ using a uniform hexahedral mesh with resolution $\triangle x = \triangle y = \triangle z = 0.001$. We solve the problem using implicit and explicit Newmark time integration schemes. For the examples that use the conditionally stable explicit scheme, with $E = 1$ GPa, $\rho = 1000$ kg m^{-3}, and $h = 0.001$ m, we obtain a wave propagation speed $c = \sqrt{\frac{E}{\rho}} = 1000$ m s^{-1}, and a stable time step estimate $\triangle t = \frac{h}{c} = 10^{-6}$ s. Nevertheless, we choose to use smaller time steps of $\triangle t = 10^{-7}$ s and $\triangle t = 10^{-8}$ s for the implicit and explicit time-integration schemes, respectively, used to advance the single-domain problem. We also consider two variants of the explicit scheme: one in which a consistent mass is used, denoted "Explicit(CM)," and one in which a lumped mass is used, denoted "Explicit(LM)." We advance the problem forward in time until a final time of $T = 1$ ms.

Table 1 reports the average z-displacement and z-velocity relative errors with respect to the exact solutions (28) and (29). The time-averaged z-displacement and z-velocity relative errors are computed using the formulas

$$\mathcal{E}_{z-\text{disp}} = \frac{1}{|\mathcal{T}_{\text{disp}}|} \sum_{t \in \mathcal{T}_{\text{disp}}} \left[\frac{\sum_z |u_3^{\text{comp}}(z, t) - u_3^{\text{exact}}(z, t)|}{\sum_z |u_3^{\text{exact}}(z, t)|} \right], \tag{31}$$

and

$$\mathcal{E}_{z-\text{vel}} = \frac{1}{|\mathcal{T}_{\text{vel}}|} \sum_{t \in \mathcal{T}_{\text{vel}}} \left[\frac{\sum_z |\dot{u}_3^{\text{comp}}(z, t) - \dot{u}_3^{\text{exact}}(z, t)|}{\sum_z |\dot{u}_3^{\text{exact}}(z, t)|} \right], \tag{32}$$

respectively. Here, $u_3^{\text{comp}}(z, t)$ and $\dot{u}_3^{\text{comp}}(z, t)$ denote the computed z-displacement and z-velocity respectively at spatial point $z \in \Omega$ and time $t > 0$; $u_3^{\text{exact}}(z, t)$ and $\dot{u}_3^{\text{exact}}(z, t)$ denote the exact analytic expressions for the z-displacement (28) and z-velocity (29) respectively at spatial point $z \in \Omega$ and time $t > 0$; finally, the $\mathcal{T}_{\text{disp}}$ and $\mathcal{T}_{\text{vel}}$ are sets of time indices over which time averaging is performed. Here, we define

$$\mathcal{T}_{\text{disp}} = \left\{ t \mid 0 \leq t \leq \left(5 \times 10^{-4}\right) - \delta, \left(5 \times 10^{-4}\right) + \delta < t \leq 1 \times 10^{-3} \right\}, \tag{33}$$

and

$$\mathcal{T}_{\text{vel}} = \left\{ t \mid 0 \leq t \leq \left(1 \times 10^{-3}\right) - 2\delta \right\}, \tag{34}$$

for $\delta > 0$, with all the corresponding times given in seconds. The reason these sets are defined in this way is to avoid the singularity in the z-displacement error at time $t = 5 \times 10^{-4}$ s and in the z-velocity error at time $t = 10^{-3}$ s. These singularities occur due to the exact solutions for the z-displacement (28) and z-velocity (29) approaching 0 at these times. In the calculations shown here, we select $\delta = 5.0 \times 10^{-6}$. The expressions $|\mathcal{T}_{\text{disp}}|$ and $|\mathcal{T}_{\text{vel}}|$ in (31) and (32) denote the cardinality of each of these sets.

The reader can observe by examining Table 1 that for the schemes considered, the time-averaged relative errors in the z-displacement and z-velocity are on the order of 0.1%–1%.

3.3.2 | Accuracy study

First, we study the accuracy of the proposed dynamic Schwarz alternating formulation for the case of a fixed domain decomposition of Ω into two subdomains: $\Omega_1 = (0, 0.001) \times (0, 0.001) \times (0, 0.75)$ and $\Omega_2 = (0, 0.001) \times (0, 0.001) \times (0.75, 1)$. The overlap volume fraction for this discretization is 50%. Let $\triangle x_i$, $\triangle y_i$, and $\triangle z_i$ denote the mesh resolutions in x, y, and z, respectively, for domain i with $i = 1, 2$. We consider the following three discretizations:

- Conformal hexahedral-hexahedral ("conformal hex-hex") coupling with $\triangle x_i = \triangle y_i = \triangle z_i = 0.001$ for $i = 1, 2$.
- Nonconformal hexahedral-hexahedral ("nonconformal hex-hex") coupling with $\triangle x_i = \triangle y_i = 0.001$ for $i = 1, 2$, $\triangle z_1 = 10^{-4}$ and $\triangle z_2 = 0.001$.
- Tetrahedral-hexahedral ("tet-hex") coupling with $\triangle x_i = \triangle y_i = \triangle z_i = 0.001$ for $i = 1, 2$.

The tetrahedral mesh in the tet-hex coupling case is generated by using a uniform hexahedral mesh and splitting each hexahedron into six tetrahedra. It is important to note that the mesh increment for all three cases considered is fine enough to resolve the propagating wave.

In addition to the three discretizations described above, we also consider three time-integration options:

- "Implicit-implicit" coupling: an implicit Newmark scheme is used in each subdomain.
- "Explicit (CM)-implicit" coupling: an explicit Newmark scheme with a consistent mass matrix is used in Ω_1 whereas an implicit Newmark scheme is used in Ω_2.
- "Explicit (LM)-implicit" coupling: an explicit Newmark scheme with a lumped mass matrix is used in Ω_1 whereas an implicit Newmark scheme is used in Ω_2.

The time-steps ($\triangle t$) utilized in all the studies are summarized in Table 2. Note that a smaller time step was used for the nonconformal hex-hex discretization solved with an explicit time-stepping scheme to ensure stability.

With the exception of the results in Table 6, we employ a very tight relative Schwarz tolerance of 10^{-15}.

TABLE 1 Baseline accuracy study for single-domain finite element discretization of Ω with a uniform mesh having resolution $\triangle x = \triangle y = \triangle z = 0.001$ m and $\triangle t = 10^{-7}$ s

	Implicit	Explicit (CM)	Explicit (LM)
Time-averaged z-disp rel error	2.78×10^{-3}	3.54×10^{-3}	3.64×10^{-3}
Time-averaged z-vel rel error	7.32×10^{-3}	9.10×10^{-3}	9.35×10^{-3}

Note: Relative errors are with respect to exact solutions (28) and (29).

TABLE 2 Time steps $\triangle t$ [s] utilized in elastic wave propagation problem studies

	Implicit-implicit	Explicit (CM)-implicit	Explicit (LM)-implicit
Conformal hex-hex	10^{-7}	10^{-7}	10^{-7}
Nonconformal hex-hex	10^{-7}	10^{-8}	10^{-8}
Tet-hex	10^{-7}	10^{-7}	10^{-7}

TABLE 3 Averaged (over times and domains) relative errors in z-displacement for the elastic wave propagation problem with several different Schwarz couplings, 50% overlap volume fraction

	Implicit-implicit	Explicit (CM)-implicit	Explicit (LM)-implicit
Conformal hex-hex	2.79×10^{-3}	3.53×10^{-3}	4.72×10^{-3}
Nonconformal hex-hex	2.90×10^{-3}	2.82×10^{-3}	2.84×10^{-3}
Tet-hex	2.79×10^{-3}	3.52×10^{-3}	4.72×10^{-3}

TABLE 4 Averaged (over times and domains) relative errors in z-velocity for the elastic wave propagation problem with several different Schwarz couplings, 50% overlap volume fraction

	Implicit-implicit	Explicit (CM)-implicit	Explicit (LM)-implicit
Conformal hex-hex	7.32×10^{-3}	8.70×10^{-3}	1.19×10^{-2}
Nonconformal hex-hex	7.10×10^{-3}	7.29×10^{-3}	7.33×10^{-3}
Tet-hex	7.58×10^{-3}	8.92×10^{-3}	1.19×10^{-2}

Tables 3 and 4 report the average (over all times and subdomains) relative errors in z-displacement and z-velocity (respectively) with respect to the exact solutions (28) and (29) (respectively) for the nine different couplings considered. These were obtained by computing the time-averaged errors within each subdomain using the formulas (31) and (32), and averaging the values among all subdomains. The reader can observe from inspecting Tables 3 and 4 that the errors in the displacement are on the order of 0.5% and the errors in the velocity are on the order of 1% for all couplings considered. These values are comparable to the errors in the single-domain baseline solution (Table 1), confirming that very little additional error, if any, is introduced by our dynamic alternating Schwarz coupling method.

Figure 3 plots the relative errors in the z-displacement and z-velocity with tet-hex, implicit-implicit coupling as a function of time t. The z-displacement relative errors at $t = 5 \times 10^{-4}$ are not shown, as the relative error at this point is not defined due to the exact solution being identically zero.

The sequence of images in Figures 4 and 5 demonstrates that the application of dynamic Schwarz coupling to the elastic wave propagation problem introduces no dynamic artifacts in displacement (Figure 4) or velocity (Figure 5) that are pervasive in other coupling methods, regardless of whether the coupling is done with different mesh resolutions, different element types like hexahedral or tetrahedral elements, or even different time integration schemes, like implicit and explicit.

3.3.3 | Convergence study

The previous subsection focused on evaluating the accuracy of the proposed dynamic Schwarz alternating formulation on the elastic wave propagation problem. Here, we turn our attention to performance.

Figure 6 shows the average number of iterations per time step as a function of the overlap volume fraction (23) for the case where two subdomains are coupled. Here, without loss of generality, each subdomain is discretized using a uniform hexahedral mesh with $\triangle x_i = \triangle y_i = \triangle z_i = 0.001$ for $i = 1, 2$, and advanced forward in time using an implicit Newmark time-integration scheme with $\triangle t = 10^{-7}$. We generate conformal hexahedral discretizations of our two subdomains having eight different overlap volume fractions, ranging from 0.2% to 100%. The details of these discretizations are summarized in Table 5. The reader can observe from examining Figure 6 that, as expected, the method converges in fewer iterations as the size of the overlap region is increased. The large relatively flat region between 5% and 80% overlap volume fraction is due to the fact that the traveling waves in this problem remain within a single subdomain for the majority of the simulation time.

Table 6 reports the maximum and average number of Schwarz iterations for a fixed overlap volume fraction of 50% using a time step of $\triangle t = 10^{-7}$ and implicit-implicit conformal hex-hex coupling as a function of the relative Schwarz tolerance.

As expected, the number of Schwarz iterations increases as the Schwarz tolerance is tightened.
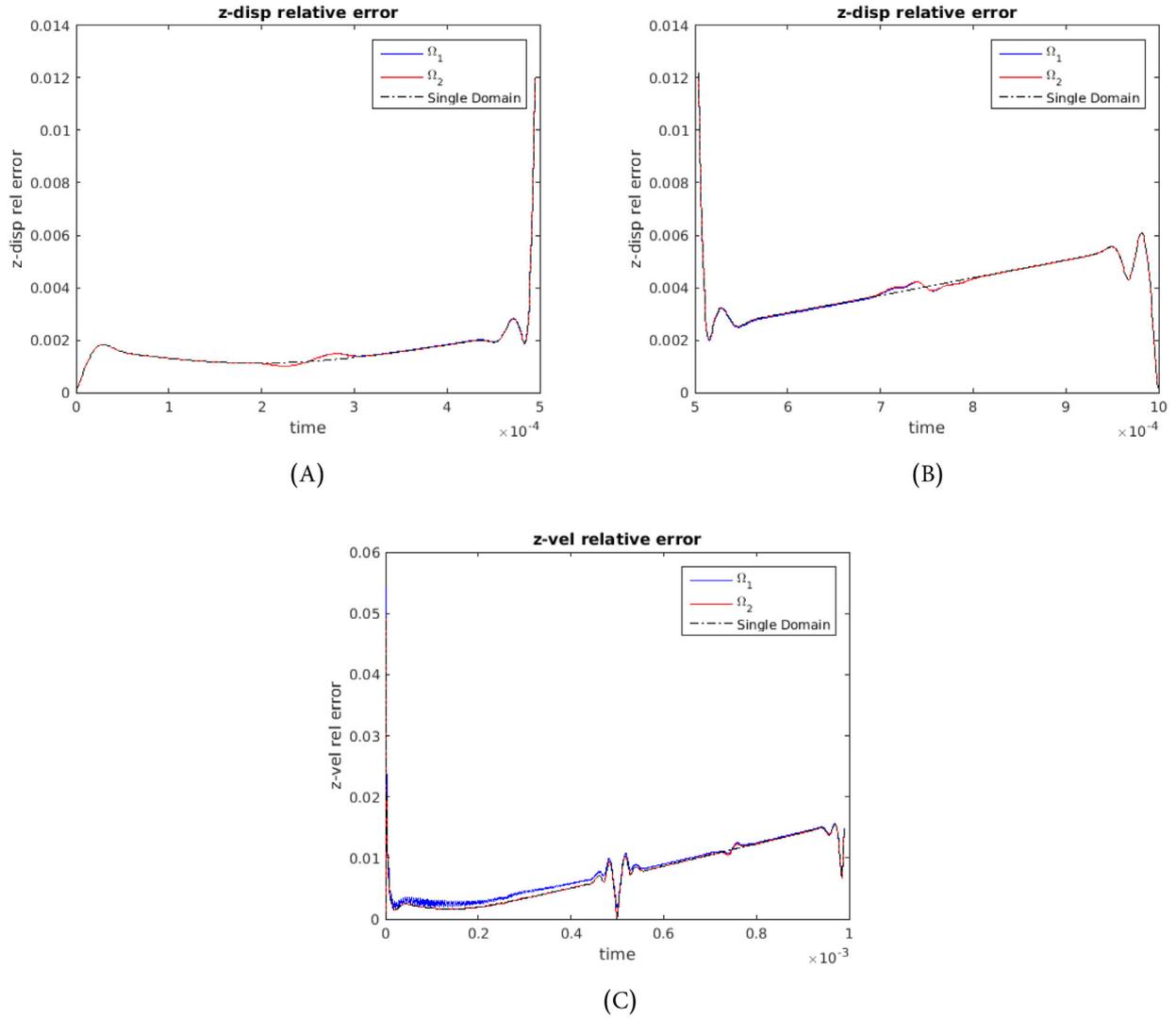
FIGURE 3 Plots of relative errors in z-displacement and z-velocity for the elastic wave propagation problem with tet-hex, implicit-implicit coupling as a function of time t, computed separately within each subdomain Ω_1 and Ω_2. z-displacement relative errors at $t = 5 \times 10^{-4}$ are not shown, as the relative error at this point is not defined due to the exact solution being identically zero. Errors are comparable to single-domain solution errors of comparable resolution for all times. (A) z-displacement error for $0 \leq t < 5 \times 10^{-4}$; (B) z-displacement error for $5 \times 10^{-4} < t \leq 1 \times 10^{-3}$; (C) z-velocity error for $0 \leq t < 1 \times 10^{-3}$

Next, we study numerically some of the convergence properties of our dynamic Schwarz method. In keeping with the convergence criterion for the Schwarz procedure proposed in Algorithm 1, we use the error measure for each Schwarz iteration

$$\epsilon^{(n)} := \left[\left(\frac{\| \triangle \boldsymbol{x}^{(n)} \|}{\| \boldsymbol{x}^{(n)} \|} \right)^2 + \left(\frac{\| \triangle \boldsymbol{x}^{(n+1)} \|}{\| \boldsymbol{x}^{(n+1)} \|} \right)^2 \right]^{1/2}, \tag{35}$$

for $n \in \{0, 2, 4, \dots \}$, where $\boldsymbol{x}$ denotes the current position, as defined earlier in Section 2. Figure 7 plots the Schwarz error measures in two subsequent Schwarz iterations, namely $\epsilon^{(n)}$ versus $\epsilon^{(n+1)}$, on a log-log scale. The figure demonstrates a monotonic linear convergence of the proposed dynamic alternating Schwarz approach. This result is similar to the one observed in Mota et al.[6] for the quasistatic version of our alternating Schwarz algorithm.
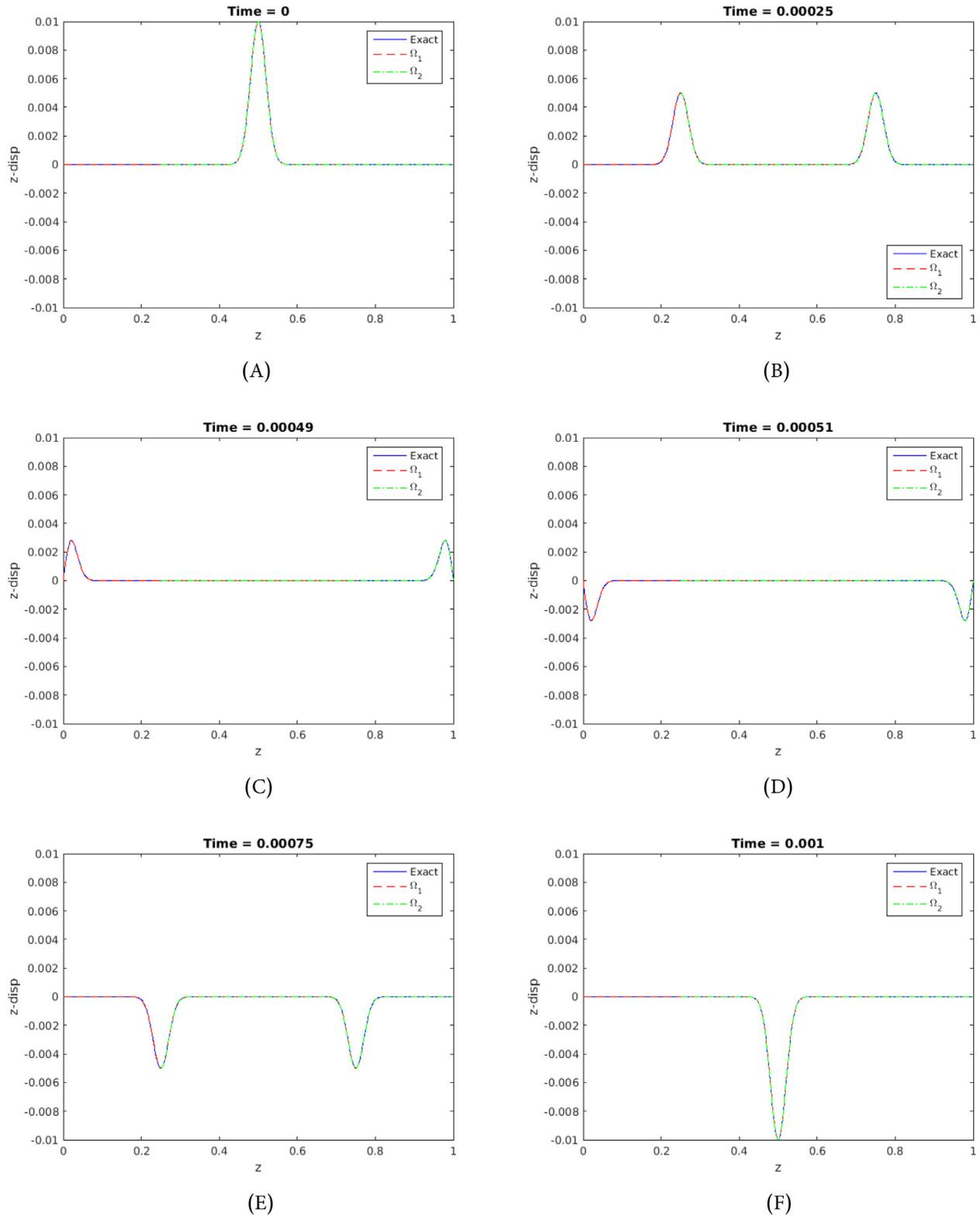
FIGURE 4 Typical snapshots of z-displacement for the elastic wave propagation problem. There are no dynamic artifacts that are pervasive in other coupling methods. (A) $t = 0$; (B) $t = 0.00025$; (C) $t = 0.00049$; (D) $t = 0.00051$; (E) $t = 0.00075$; (F) $t = 0.001$
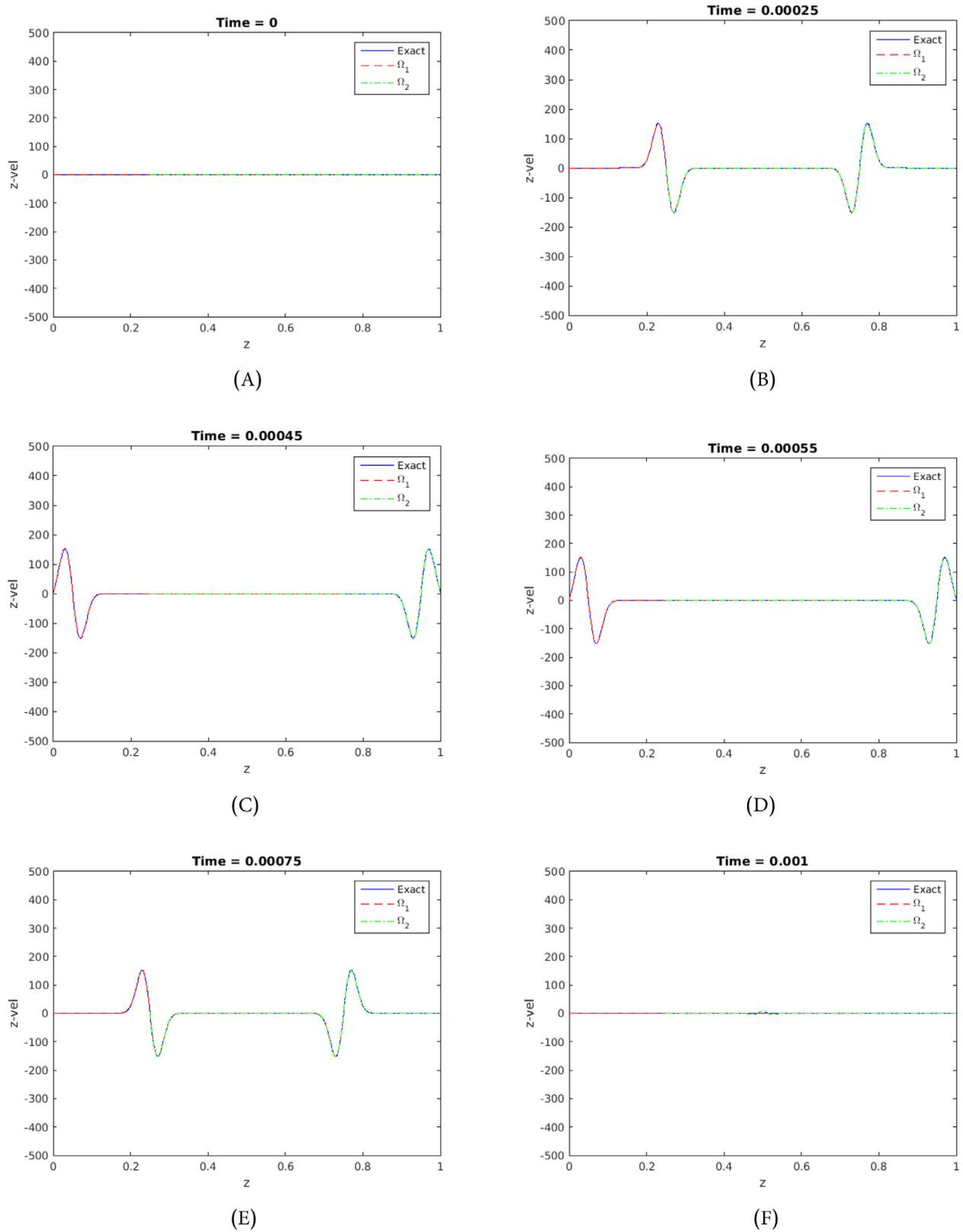
FIGURE 5 Typical snapshots of z-velocity for the elastic wave propagation problem. There are no dynamic artifacts that are pervasive in other coupling methods. (A) $t = 0$; (B) $t = 0.00025$; (C) $t = 0.00045$; (D) $t = 0.00055$; (E) $t = 0.00075$; (F) $t = 0.001$
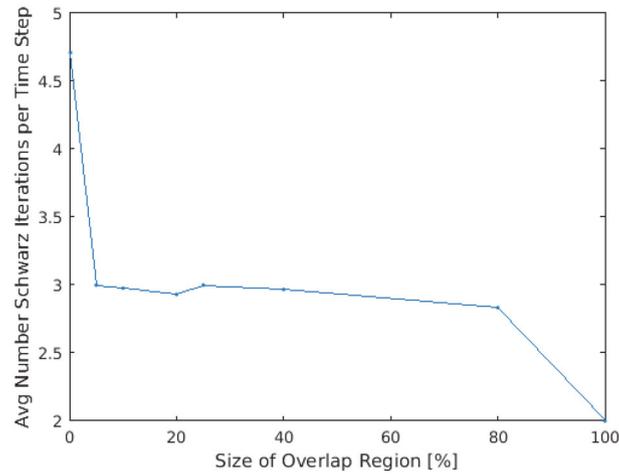
FIGURE 6 Average number of Schwarz iterations per time step as a function of the overlap volume fraction for the elastic wave propagation problem for a fixed relative Schwarz tolerance of 10^{-15}. As expected, the method does not converge for 0% overlap. If the overlap is 100%, then the single domain solution is recovered for each of the subdomains

TABLE 5 Summary of the eight discretizations employed in our study of the effect of the size of the overlap volume region on convergence for the elastic wave propagation problem

Overlap volume fraction	$\Omega_{z,1}$	$\Omega_{z,2}$
0.2%	$(0, 0.501)$	$(0.499, 1)$
5%	$(0, 0.525)$	$(0.475, 1)$
10%	$(0, 0.55)$	$(0.45, 1)$
20%	$(0, 0.6)$	$(0.4, 1)$
25%	$(0, 0.625)$	$(0.375, 1)$
40%	$(0, 0.7)$	$(0.3, 1)$
80%	$(0, 0.8)$	$(0.2, 1)$
100 %	$(0, 1)$	$(0, 1)$

Note: Here, $\Omega_{z,i}$ is the size of Ω_i in the z-direction, so that $\Omega_i = (0, 0.001) \times (0, 0.001) \times \Omega_{z_i}$ for $i = 1, 2$. Each subdomain is discretized using a uniform hexahedral mesh with $\triangle x_i = \triangle y_i = \triangle z_i = 0.001$ for $i = 1, 2$.

TABLE 6 Average and maximum number of Schwarz iterations for the conformal hex-hex coupling discretization of the elastic wave propagation problem as a function of the relative Schwarz tolerance, assuming implicit-implicit coupling with $\triangle t = 10^{-7}$ s and an overlap volume fraction of 50%

Schwarz tolerance	10^{-6}	10^{-10}	10^{-15}
Average # Schwarz iterations	2.08	2.38	2.83
Maximum # Schwarz iterations	3	3	4

3.3.4 | Different time integrators and time steps

In this subsection we demonstrate the ability of the Schwarz method to couple subdomains using different time integrators and also different time steps. Figure 8 shows a typical plot of displacement, velocity and acceleration for the elastic wave propagation problem using different time integrators (implicit and explicit) and different time steps (2×10^{-7} s and 1×10^{-2} s) for each subdomain, superimposed over the analytic solution. The controller time step in this case is set to 2×10^{-7} s. These results demonstrate that our dynamic Schwarz implementation enables the use of not only different time integrators within different subdomains, but also different time steps. Moreover, the use of different time-steps does
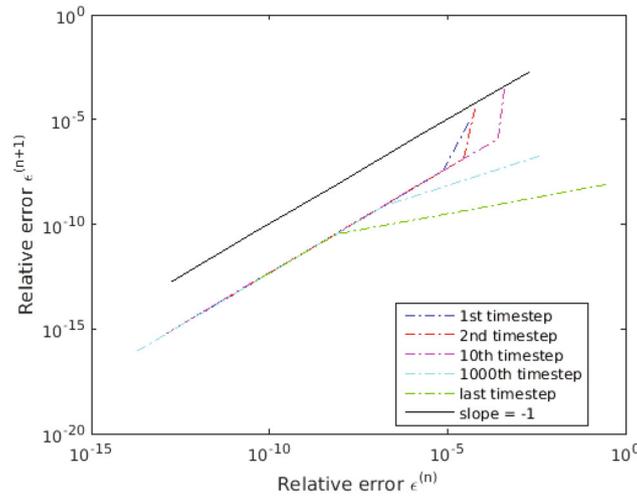
FIGURE 7 Convergence behavior of the dynamic Schwarz algorithm for the elastic wave propagation problem with a small overlap volume fraction (0.2%) for $n = 0, 1, \ldots, N_{iter} - 1$, where N_{iter} is the number of Schwarz iterations required for convergence in a given controller time step. The plot shows that a linear convergence rate is achieved

not introduce into the computation spurious errors or artifacts. We note that the use of different time steps in different subdomains requires a slightly more intrusive computer implementation, as one needs to store the solution history of each subdomain within the controller time step as well as interpolate solutions in time for the application of the Schwarz boundary conditions.

In our MATLAB prototype code, the implementation of multiple step time integrators is relatively trivial. For each controller step as defined in Figure 1, the history of solutions for each subdomain is stored. For example, using Figure 1 as reference, one would need to store three solutions for the red circle and four solutions for the green rectangle for each controller step. For this one-dimensional problem, MATLAB provides a convenient function called *interp2* that is able to perform interpolation in space and time simultaneously. In this way, each subdomain is able to advance using its own time step, and when information is required from another subdomain for the application of a boundary condition, it is obtained by means of the *interp2* function. For a general finite element code, this functionality would need to be reproduced if this capability is desired.

3.4 | Torsion

In the next test case, evaluated within the ALBANY LCM code, we consider a hyperelastic bar subjected to finite deformation by a high degree of torsion. The geometry is given by $\Omega = (-0.025, 0.025) \times (-0.025, 0.025) \times (-0.5, 0.5)$. The initial condition corresponds one of torsion about the $z = 0$ axis:

$$\boldsymbol{u}(\boldsymbol{x}, 0) = \boldsymbol{0},$$
$$\dot{\boldsymbol{u}}(\boldsymbol{x}, 0) = (-ayz, axz, 0), \tag{36}$$

where $a = 8000$, $\boldsymbol{u}$ is the displacement vector, and $\dot{\boldsymbol{u}}$ is the velocity vector. The boundary conditions are all homogeneous Neumann. We specify a Neohookean-type material model with Young's modulus $E = 1.0 \times 10^9$ GPa, Poisson's ratio $\nu = 0.25$ and density $\rho = 1000$ kg/m^3. The problem is run until time $T = 2 \times 10^{-3}$ s. In order to resolve the solution, the time step employed in the time-integration scheme, $\triangle t$, must satisfy $\triangle t \leq h/c$, where h is a measure of the mesh spatial resolution, and c is the relevant wave propagation speed, given by $c = \max\left(\sqrt{E/\rho}, \sqrt{G/\rho}, \sqrt{K/\rho}\right)$ where E is the Young's modulus, G is the shear modulus, K is the bulk modulus, and ρ is the solid density. For this torsion problem, with $E = 1$ GPa, $\nu = 0.25$ and $\rho = 1000$ kg m^{-3}, the relevant wave propagation speed is $c = 1000$ m s^{-1}. The minimum element size used is $h = 0.0045$ m, therefore the stable time step is $\triangle t = \frac{h}{c} = 4.5 \times 10^{-6}$ s. We simply choose to use $\triangle t = 10^{-6}$ s as being sufficiently close to the estimate and to more easily track the output.
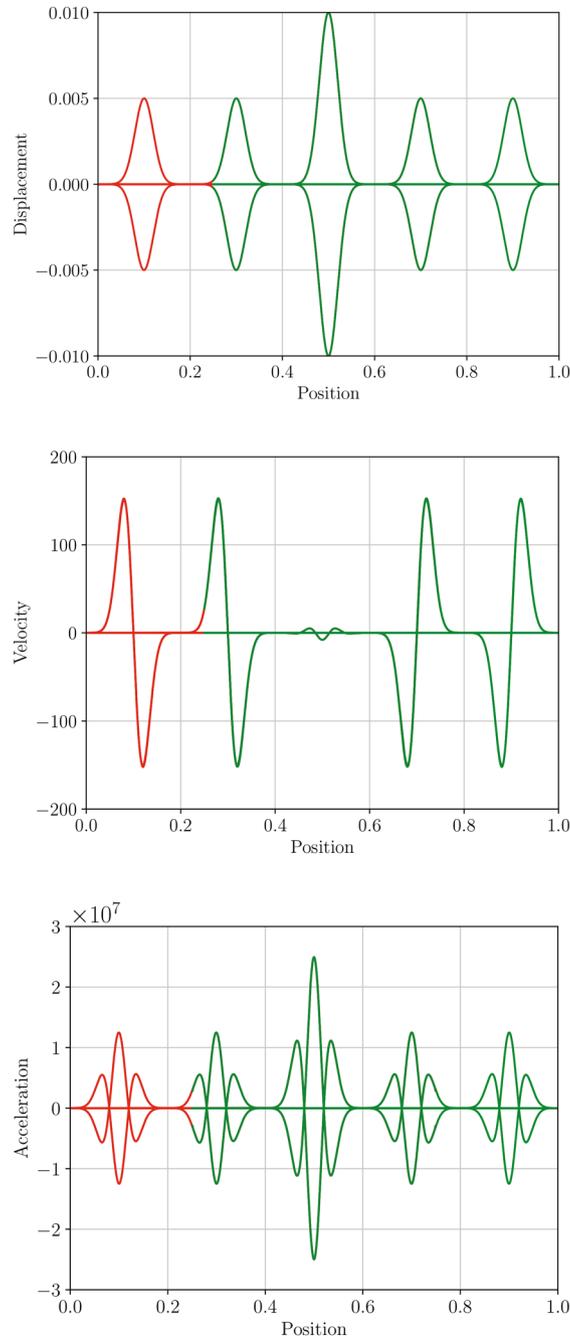
FIGURE 8 Typical plot of displacement, velocity, and acceleration for the elastic wave propagation problem using different time integrators (implicit and explicit) and different time steps (2×10^{-7} and 1×10^{-7} s) for each subdomain, superimposed over the analytic single domain solution. Overlapped plots shown at $t = (0, 2, 4, 6, 8, 10) \times 10^{-4}$ s. The analytic solution is hidden behind the solutions for Ω_1 (red) and Ω_2 (green)

The main purpose of this case is to demonstrate that the dynamic Schwarz method can be used to couple two regions of the bar using different mesh resolutions, different element types, and different time integration schemes, once more without introducing any dynamic artifacts.

3.4.1 | Conformal hex-hex coupling

In our first study, we investigate the error introduced by our dynamic alternating Schwarz formulation while removing other sources of error as much as possible. To this end, we consider a domain decomposition of the geometry
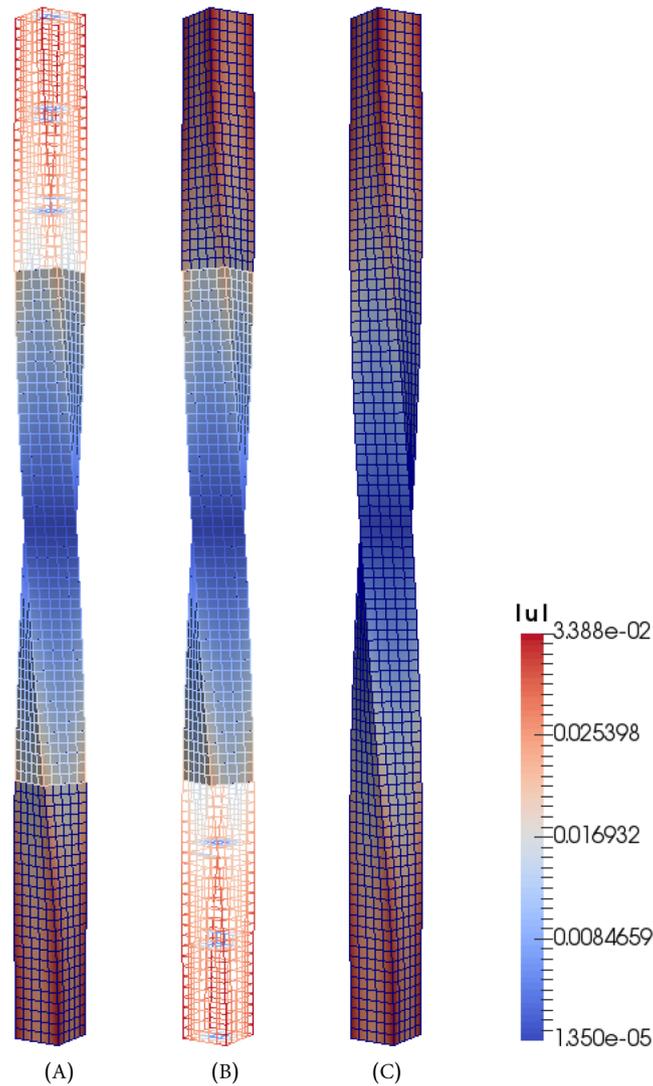
FIGURE 9 Comparison of the solution for the coupled torsion problem with respect to a single-domain solution. The color scheme shows the norm of the displacement vector $|u|$ at the final time step computed on Ω_1 with 1875 hexahedral elements in (A) and Ω_2 with 1875 hexahedral elements in (B). The reference single-domain solution on Ω_{ref} with 2500 hexahedral elements is shown in (C). All meshes are conformal

Ω into two subdomains Ω_1 and Ω_2 in which the subdomains are discretized using conformal hexahedral meshes. Let $\Omega_1 = (-0.025, 0.025) \times (-0.025, 0.025) \times (-0.5, 0.25)$ and $\Omega_2 = (-0.025, 0.025) \times (-0.025, 0.025) \times (-0.25, 0.5)$. We discretize each domain with a uniform hexahedral mesh with mesh size $\triangle x = \triangle y = \triangle z = 0.01$, see Figure 9A,B. We apply our dynamic Schwarz method to solve this problem and compare the result to a single-domain solution discretized using the same uniform mesh resolution, shown in Figure 9C. We utilize an implicit Newmark time-integration scheme with time step $\triangle t = 1 \times 10^{-6}$ s to compute the Schwarz as well as the single-domain solutions. Figure 9 shows the magnitude of the displacement at the final time. The solutions obtained using the Schwarz method in each of the two domains (Figure 9A,B) are indistinguishable from the single domain solution (Figure 9C). Indeed, Figures 10 and 11 show the errors in the displacement and velocity respectively at the final time, which are close to machine precision. Since the Schwarz meshes and the single-domain mesh are conformal, it is straightforward to compute relative errors in the Schwarz solutions with respect to the single domain solution simply by subtracting the solutions at the nodes and taking an l_2 vector norm of this difference.

Figure 12A,B show a time-history of the relative error in the displacement and velocity magnitudes, respectively. The reader can observe that the maximum error is $\mathcal{O}(10^{-11})$. This demonstrates that, in the absence of other sources of
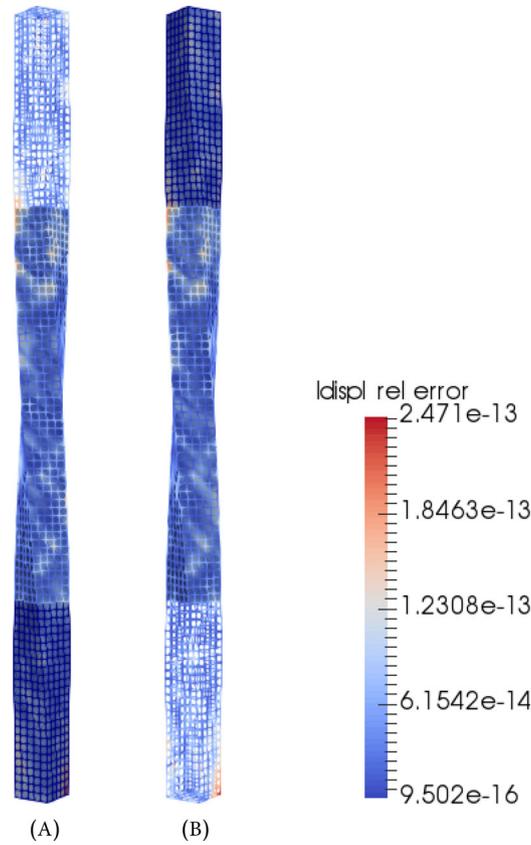
FIGURE 10 Relative errors in the norm of the displacement for the coupled torsion problem discretized using conformal hexahedral meshes with respect to a single-domain solution at the final time $T = 2 \times 10^{-3}$ s. Errors are close to machine precision. (A) Ω_1; (B) Ω_2

error such as geometric error, the error in the coupling using our Schwarz formulation can be decreased up to numerical precision. Spikes in the displacement and velocity relative errors are observed near times where the reference solution magnitude is close to zero[¶].

3.4.2 | Nonconformal composite tet-hex coupling

After verifying that the coupling errors of our dynamic Schwarz method are close to machine precision in the case of conformal coupling, where no other source of error (such as geometric mismatch) exist, we now evaluate this formulation on the torsion problem in the case Ω_1 and Ω_2 are discretized using nonconformal meshes with different element types. Toward this end, let us define the following domain decomposition of Ω: $\Omega = \Omega_1 \cup \Omega_2$, where $\Omega_1 = (-0.025, 0.025) \times (-0.025, 0.025) \times (-0.5, 0.22)$ and $\Omega_2 = (-0.025, 0.025) \times (-0.025, 0.025) \times (-0.22, 0.5)$. First, we discretize Ω_1 with a uniform hexahedral mesh with mesh sizes $\triangle x_1 = \triangle y_1 = 0.01$ and $\triangle z_1 = 0.012$, resulting in a mesh with 1500 hexahedral elements. Similarly, we discretize Ω_2 with a uniform hexahedral mesh with mesh sizes $\triangle x_2 = \triangle y_2 = 0.005$ and $\triangle z_2 = 0.0045$, resulting in a mesh with 16,000 hexahedral elements. Since we wish to employ different element types in different subdomains, we create a 10-node composite tetrahedron ("composite tet")[54] mesh of Ω_1 by splitting each hexahedral element in this mesh into 6 tetrahedra, and enriching this mesh with additional nodes. The resulting mesh consists of 9000 10-node composite tet elements. The decomposition and their corresponding discretizations are shown in Figure 13A,B. We evaluate the accuracy in the solutions obtained by our dynamic Schwarz coupling method by computing errors with respect to a reference solution discretized using 20,000 hexahedral elements with mesh size $\triangle x = \triangle y = \triangle z = 0.005$ (Figure 13C). The resolution of Ω is roughly comparable to that of Ω_1 and Ω_2; we emphasize, however, that none of the meshes considered are conformal with each other, that is, they do not share any nodes.
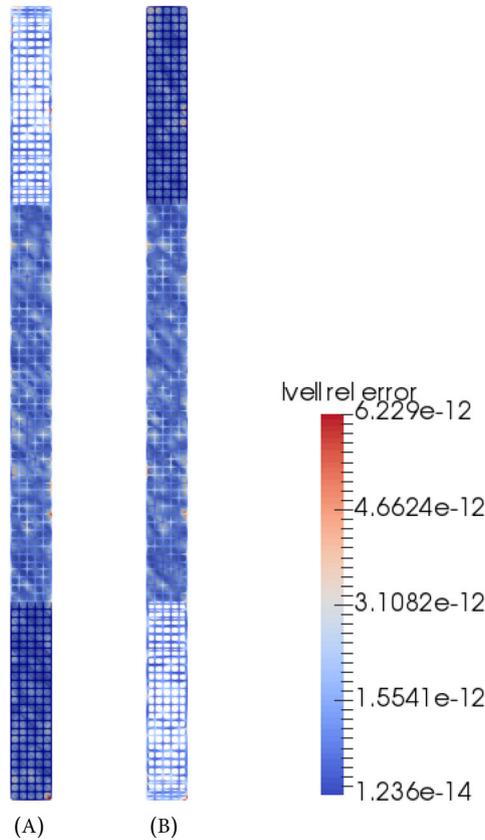
FIGURE 11   Relative errors in the norm of the velocity for the coupled torsion problem discretized using conformal hexahedral meshes with respect to a single-domain solution at the final time $T = 2 \times 10^{-3}$ s. Errors are close to machine precision. (A) Ω_1; (B) Ω_2

We study the accuracy in the proposed nonconformal Schwarz coupling of meshes with different element types. As with the elastic wave problem considered in Section 3.3, we consider three time-integration options:

- "Implicit-implicit" coupling: an implicit Newmark scheme is used in each subdomain.
- "Explicit (CM)-implicit" coupling: an explicit Newmark scheme with a consistent mass matrix is used in Ω_1 whereas an implicit Newmark scheme is used in Ω_2.
- "Explicit (LM)-implicit" coupling: an explicit Newmark scheme with a lumped mass matrix is used in Ω_1 whereas an implicit Newmark scheme is used in Ω_2.

For all time-integration schemes, a time step of $\triangle t = 1 \times 10^{-6}$ is employed. This time step is stable and small enough to resolve the torsion behavior in the bar.

Tables 7 and 8 give the relative errors in the displacement and velocity norms, respectively, in the solutions obtained using our nonconformal Schwarz coupling method with the three integrators considered at four representative times during the simulation. These errors were calculated using the `DTK_Interp_and_Error` utility within ALBANY LCM, described earlier in Section 3.2. Each entry in the tables contains the average relative error, with the averaging performed over the two subdomains considered. These tables show that, for the implicit-implicit and explicit (CM)-implicit time-discretizations, the errors in the Schwarz solutions are $\mathcal{O}(0.1)\%$ for the displacement and $\mathcal{O}(1)\%$ for the velocity. For the errors in the explicit (LM)-implicit time-discretization, the errors in the Schwarz solution are up to an order of magnitude higher. This is due to the fact that mass lumping introduces some error into the simulation, which accumulates and leads to a slight difference in phase between the two subdomains. Figure 14 shows a time-history of the relative errors in the Schwarz displacement (a) and velocity (b) solutions obtained using the nonconformal composite tet-hex implicit-implicit coupling. The reader can observe that the relative errors are at $< 5\%$ for most times. As for the conformal hex-hex coupling variant of this problem,
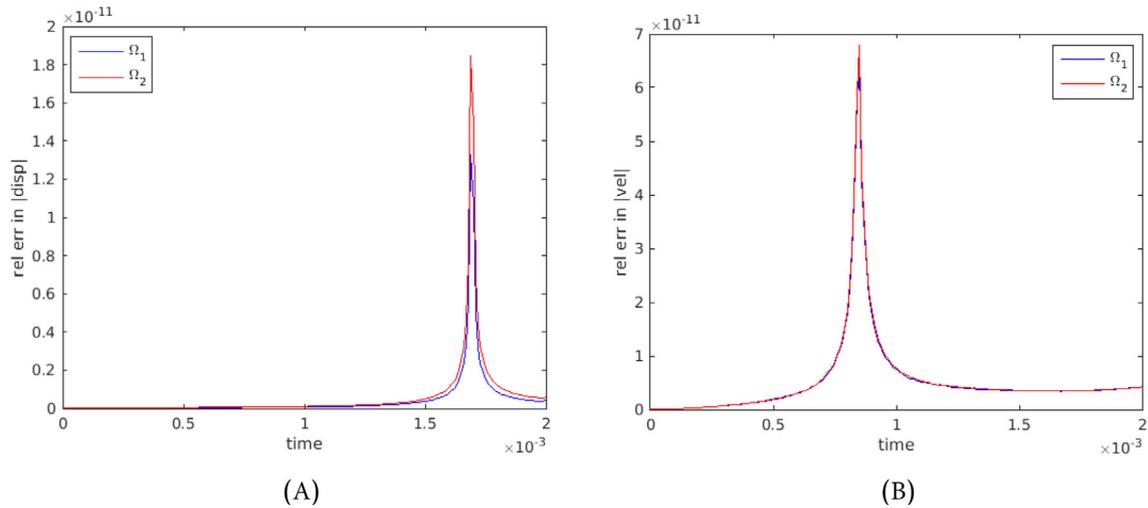
FIGURE 12 Time history of the relative errors in the norm of the displacement and velocity for the coupled torsion problem discretized using conformal hexahedral meshes with respect to a single-domain solution. Errors are at most $\mathcal{O}(10^{-11})$. Spikes in the displacement and velocity relative errors are observed near times where the reference solution magnitude is close to zero. (A) Relative errors in displacement; (B) Relative errors in velocity

spikes in the displacement and velocity relative errors are observed near times where the reference solution magnitude is close to zero. The time-values at which relative errors are reported in Tables 7 and 8 are marked by circles.

3.4.3 | Convergence study

Figure 15 plots the Schwarz error measures in two subsequent Schwarz iterations, namely $\epsilon^{(n)}$ versus $\epsilon^{(n+2)}$ as defined in (35), on a log-log scale. The overlap volume fraction for this study is 2%, which is much smaller than the one in the studies discussed above, with $\Omega_1 = (-0.025, 0.025) \times (-0.025, 0.025) \times (-0.5, 0.01)$ and $\Omega_2 = (-0.025, 0.025) \times (-0.025, 0.025) \times (-0.01, 0.5)$. Both subdomains are discretized using conformal hexahedral meshes with uniform mesh resolutions of $\triangle x_i = \triangle y_i = \triangle z_i = 0.01$ for $i = 1, 2$. We reduce the overlap for the convergence study in order to stress-test the method and to demonstrate that it converges even in the case of a very small overlap. The reader can observe that the method is converging monotonically at a linear rate of convergence, similar to what was observed for the problem in Section 3.3. These results are consistent with what is reported in Section 3.3.3 for the elastic wave propagation problem and in Mota et al.[6] for our quasistatic variant of Schwarz coupling.

Table 9 reports the average number of Schwarz iterations per time step for some of the different discretizations discussed above, each with an overlap volume fraction of close to 50%. One can see that a small number (3–4) of Schwarz iterations are required to achieve convergence. It is interesting to observe that more Schwarz iterations are required when employing an explicit time-integration scheme with a lumped mass in one of the subdomains.

3.5 | Bolted joint

We conclude our numerical experiments by applying the proposed dynamic alternating Schwarz method to a realistic problem that is of interest to us, which highlights the "plug-and-play" nature of this coupling approach as used with the SIERRA code.[52] We will refer to as a bolted joint problem. Bolted joints are ubiquitous in machine design and engineered structures encountered in daily life (e.g., the light post in Figure 16A). They consist of small-scale fasteners or bolts which join together other, larger-scale components.
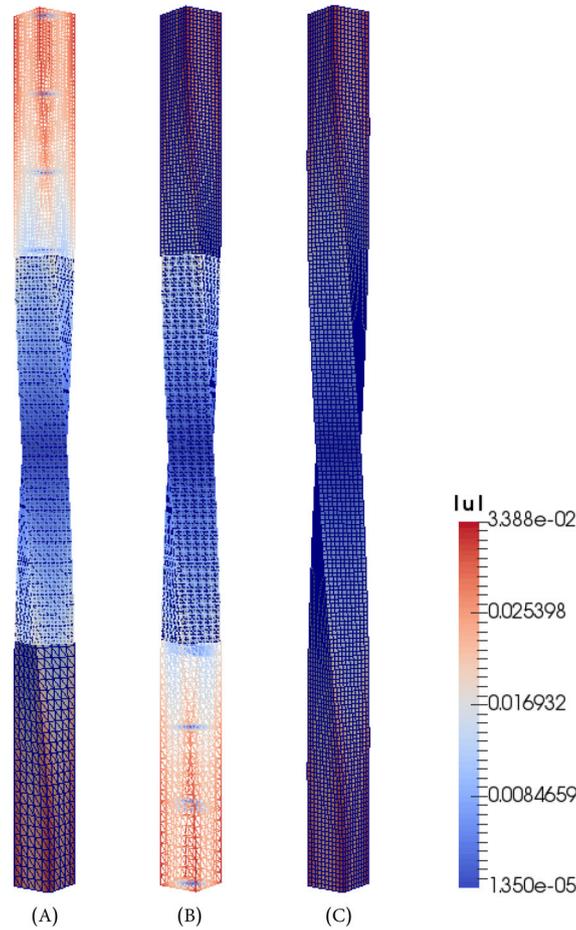
FIGURE 13 Comparison of the solution for the coupled torsion problem, where Ω_1 is discretized using a composite tet mesh with 16,000 elements, and Ω_2 is discretized using a hex mesh with 9000, with respect to a single-domain solution obtained on a fine (20,000 element) hexahedral mesh. The color scheme shows the norm of the displacement vector $|\boldsymbol{u}|$ at the final time step. All meshes are non-conformal. Without loss of generality, we show here only the solution computed using implicit Newmark time steppers within each subdomain. (A) Ω_1; (B) Ω_2; (C) Ω_{ref}
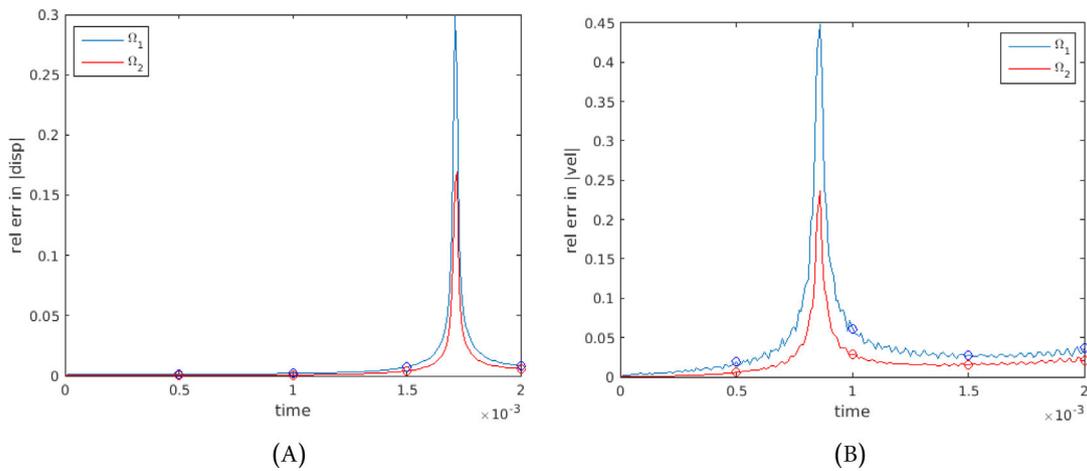
FIGURE 14 Time history of the relative errors in the norm of the displacement and velocity for the coupled torsion problem discretized using nonconformal meshes (a composite tet mesh in Ω_1 and a hexahedral mesh in Ω_2) with respect to a fine single-domain solution. Without loss of generality, we show here only the errors for solutions obtained using implicit Newmark time steppers within each subdomain. Relative errors are at $< 5\%$ for most times. Spikes in the displacement and velocity relative errors are observed near times where the reference solution magnitude is close to zero. The time-values at which relative errors are reported in Tables 7 and 8 are marked by circles. (A) Ω_1; (B) Ω_2

TABLE 7 Comparison of relative errors in displacement norm for the torsion problem discretized using the Schwarz method with nonconformal composite tet-hex coupling and different time-integration schemes with respect to a single-domain fine reference solution

	Relative error in displacement norm			
	$t = 5 \times 10^{-4}$	$t = 1 \times 10^{-3}$	$t = 1.5 \times 10^{-3}$	$t = 2 \times 10^{-3}$
Implicit-implicit	7.96×10^{-4}	1.28×10^{-3}	5.68×10^{-3}	7.23×10^{-3}
Explicit (CM)-implicit	1.09×10^{-3}	1.93×10^{-3}	8.19×10^{-3}	8.21×10^{-3}
Explicit (LM)-implicit	3.66×10^{-3}	1.62×10^{-2}	7.13×10^{-2}	6.14×10^{-2}

Note: At each time, the reported errors are an average of the errors over the two subdomains.

TABLE 8 Comparison of relative errors in velocity norm for the torsion problem discretized using the Schwarz method with nonconformal composite tet-hex coupling and different time-integration schemes with respect to a single-domain fine reference solution

	Relative error in velocity norm			
	$t = 5 \times 10^{-4}$	$t = 1 \times 10^{-3}$	$t = 1.5 \times 10^{-3}$	$t = 2 \times 10^{-3}$
Implicit-implicit	1.27×10^{-2}	4.50×10^{-2}	2.09×10^{-2}	2.89×10^{-2}
Explicit (CM)-implicit	1.30×10^{-2}	4.63×10^{-2}	2.13×10^{-2}	2.89×10^{-2}
Explicit (LM)-implicit	4.59×10^{-2}	1.60×10^{-1}	5.91×10^{-2}	6.72×10^{-2}

Note: At each time, the reported errors are an average of the errors over the two subdomains.
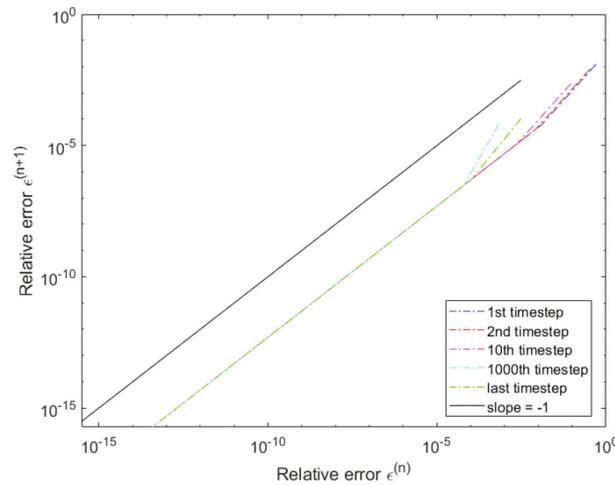
FIGURE 15 Convergence behavior of the dynamic Schwarz algorithm for the torsion problem with a small overlap volume fraction (2%) for $n = 0, 1, \ldots, N_{\text{iter}} - 1$, where N_{iter} is the number of Schwarz iterations required for convergence in a given controller time step. In this instance of the problem, each subdomain is discretized using a hexahedral mesh. The plot shows that a linear convergence rate is achieved

TABLE 9 Average number of Schwarz iterations per time step

	Conformal hex-hex	Nonconformal composite tet-hex
Overlap volume fraction	44%	50%
Implicit-implicit, explicit (CM)-implicit	3	3
Explicit (LM)-implicit	4	4
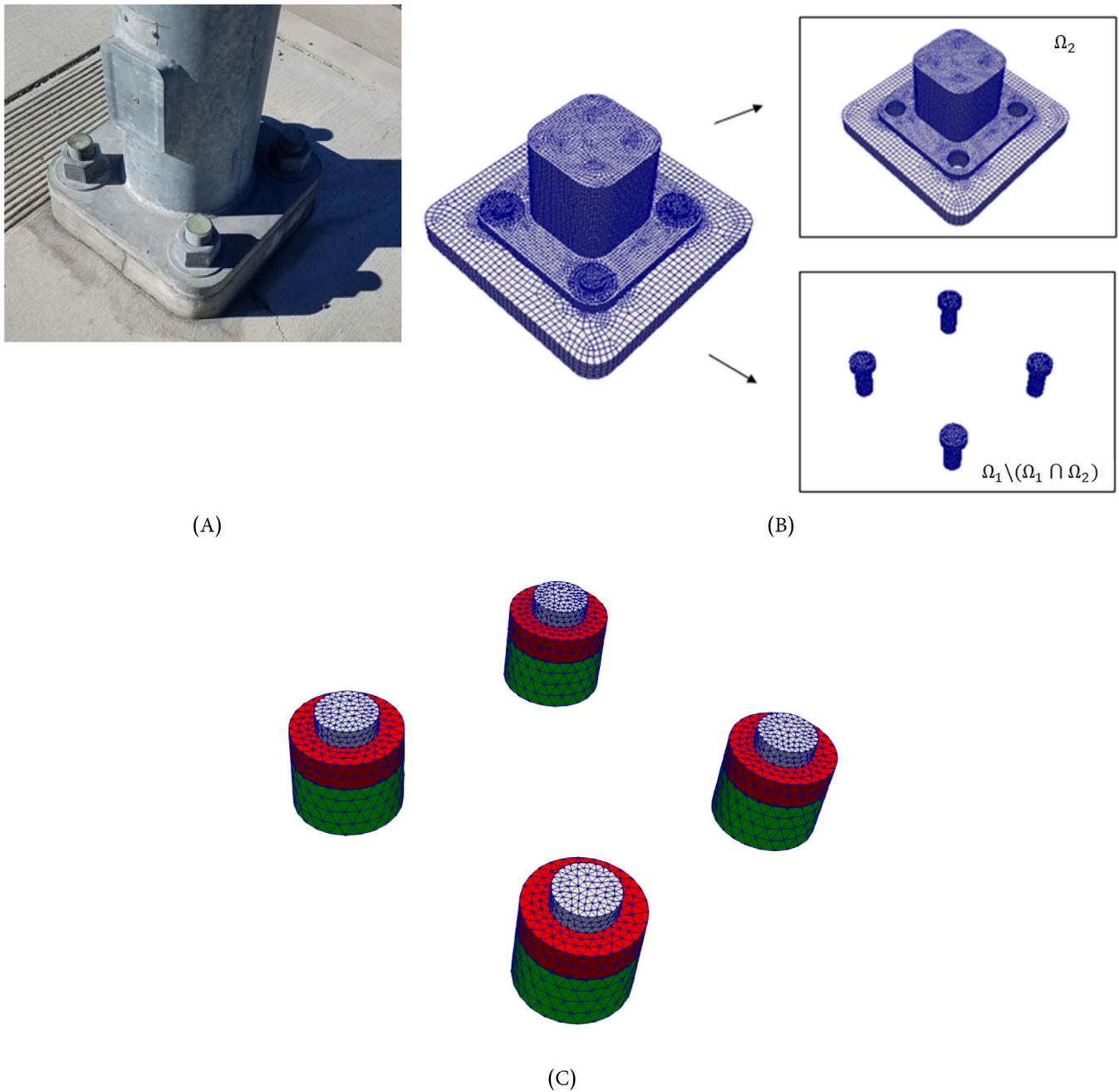
FIGURE 16 Depiction of bolted joint geometry physical model and its CAD model analog, along with a domain decomposition into two subdomains, Ω_1 and Ω_2 for the application of Schwarz, and meshing of each subdomain. Ω_1 and Ω_2 are referred to as the "bolts" an the "parts," respectively. For the application of Schwarz, we discretize Ω_1 with a composite tetrahedral mesh and Ω_2 with a hexahedral mesh. Subfigure (C) depicts Ω_1 together with the overlap region, colored in red and green. (A) Example physical model; (B) CAD model, domain decomposition and meshing of physical model; (C) Bolts with overlap region (Ω_1)

The computer-aided design (CAD) model considered here (Figure 16B) is comprised of three pieces: a bottom aluminum plate, a top steel (FC0205) component, and four high-strength steel (8740) bolts, which join together the plate and the component. The material properties are shown in Table 10. The overall dimensions of the joint are a square base of 127 mm × 127 mm, and a height of 127 mm. We prescribe a finite deformation J_2 material with linear hardening within the model.

In applying the Schwarz method, a natural domain decomposition of the geometry is into two subdomains, one containing the four bolts and one containing the so-called "parts," which consist of the bottom plate and the top

component (Figure 16). The intention of this problem is to demonstrate the application of the Schwarz method to a production-like problem, as well as to highlight the "plug-and-play" nature of the method: if one is interested in changing the shape the parts and/or including more detail in the bolts (e.g., by adding threading), one can create these new models offline and apply the Schwarz method to the new geometry. It is similarly easy to replace the meshes and/or material models employed in the simulation. For more complex geometries, one can craft a domain decomposition that will facilitate generating meshes for the separate subdomain geometries, thereby circumventing the task of having to remesh a complex realistic geometry, a task which can take *weeks*. Figure 16C depicts Ω_1 together with the overlap region, which contains a piece of the "parts" and bottom plate, shown in red and green, respectively. Remark that the domain decomposition is done such that the overlap region is quite small relative to the overall volume of the considered geometry.

In this domain decomposition, it is natural to discretize the parts with a relatively coarse mesh, while representing the bolts with a fine mesh. A fine mesh representation of the bolts is particularly important in the case that the bolts are threaded.

In the study summarized herein, the discretized parts domain is labeled Ω_2 and discretized using an 8-node hexahedral mesh having a total of 38,728 elements. To test the "plug-and-play" nature of the proposed Schwarz formulation, we consider two meshes for the bolts, labeled Ω_1^f and Ω_1^c, defined as $\Omega_1 \setminus (\Omega_1 \cap \Omega_2)$ for the fine and coarse discretizations of the bolts, respectively. Both of these meshes are comprised of 10-node composite tetrahedral elements.[54] The former discretization has 15,576 such elements whereas the latter has 132,060 such elements. We compare our Schwarz solution with a solution computed on a single-domain mesh of the geometry, which we will denote by Ω^c. This mesh of Ω^c is comprised of 118,619 composite tetrahedral elements, 17,238 of which are used to discretize the bolts. The meshes considered are shown in Figure 17. The total element and node counts for the various discretizations considered are summarized in Table 11.

We prescribe a zero displacement boundary condition on the bottom boundary of Ω_2. Meanwhile, at the top boundary of Ω_2 we apply a time-dependent x-displacement:

$$u_1(\boldsymbol{x}, t) = 2t, \quad t \geq 0, \boldsymbol{x} \in \Omega_2. \tag{37}$$

We assume the initial displacement and velocities are identically zero within both subdomains. We advance the problem forward in time using an implicit Newmark scheme with a simple time-step control algorithm up to a final time of $T = 8.0 \times 10^{-4}$ s. The time-step control algorithm effectively reduces the time-step by a reduction factor r if convergence is not achieved within a time-step; alternatively, the time-step is increased by an amplification factor a. For the runs described here, we take $r = 0.5$ and $a = 1.1$. We take the initial time steps for the single-domain and Schwarz runs to be $\Delta t = 1.0 \times 10^{-6}$ s. Given the strong nonlinearity implied by the prescribed (inelastic) material model, we employ a relative tolerance of 1.0×10^{-8} on the residual within our Newton nonlinear solver. For the Schwarz runs, we utilize a relative Schwarz tolerance of 1.0×10^{-6}.

Figure 18 shows the x-component of the displacement for the three runs considered at time $t = 4.87 \times 10^{-4}$ s. The reader can observe that the geometry has undergone significant deformation. Moreover, the Schwarz solutions (Figure 18A,B) are indistinguishable from the single-domain solution (Figure 18C). Moreover, the deformation exhibited by the numerically computed solutions is similar in nature to a real-world reference geometry (Figure 18D).

In addition to the x-displacement, we compare also the nodal equivalent plastic strain (eqps), computed via a weighted volume average within the ALBANY code, in the bolts. This quantity is plotted for all three runs in Figures 19 and 20. Figure 20 depicts a vertical slice through the bolts (Figure 20). The reader can observe higher strain concentrations within the bolts at the locations where failure is expected for the Schwarz solution with the finer mesh of the bolts Ω_1^f (Figure 20C), which has almost ten times the number of elements within the bolts subregion compared to the single-domain mesh (132,060 composite tetrahedra vs. 17,238). The Schwarz solution with the coarser mesh of the bolts Ω_1^c (Figure 20B) matches well the single domain solution (Figure 20A). This is because the meshes within the bolts are comparable in resolution: 15,576 composite tetrahedra for Schwarz versus 17,238 composite tetrahedra for the single-domain (Figure 21).

To achieve convergence to the specified relative Schwarz tolerance of 1.0×10^{-6}, only 2-4 iterations per time-step were required for both Schwarz runs shown herein. As one would expect, the number of Schwarz iterations increased as the simulation progressed and the geometry deformed (Figure 22). Table 12 summarizes some of the convergence and performance data for the Schwarz runs considered, compared to two single domain runs. Both single

TABLE 10 Material properties for the bolted joint example

Material	Young's modulus (GPa)	Poisson's ratio	Yield strength (MPa)	Hardening modulus (GPa)	Density (kg m^{-3})
Aluminum	70	0.36	250	0.70	2700
FC0205 steel	200	0.30	350	8.00	7800
8740 steel	200	0.30	1000	0.15	7800

(A)

(B)

(C)

(D)
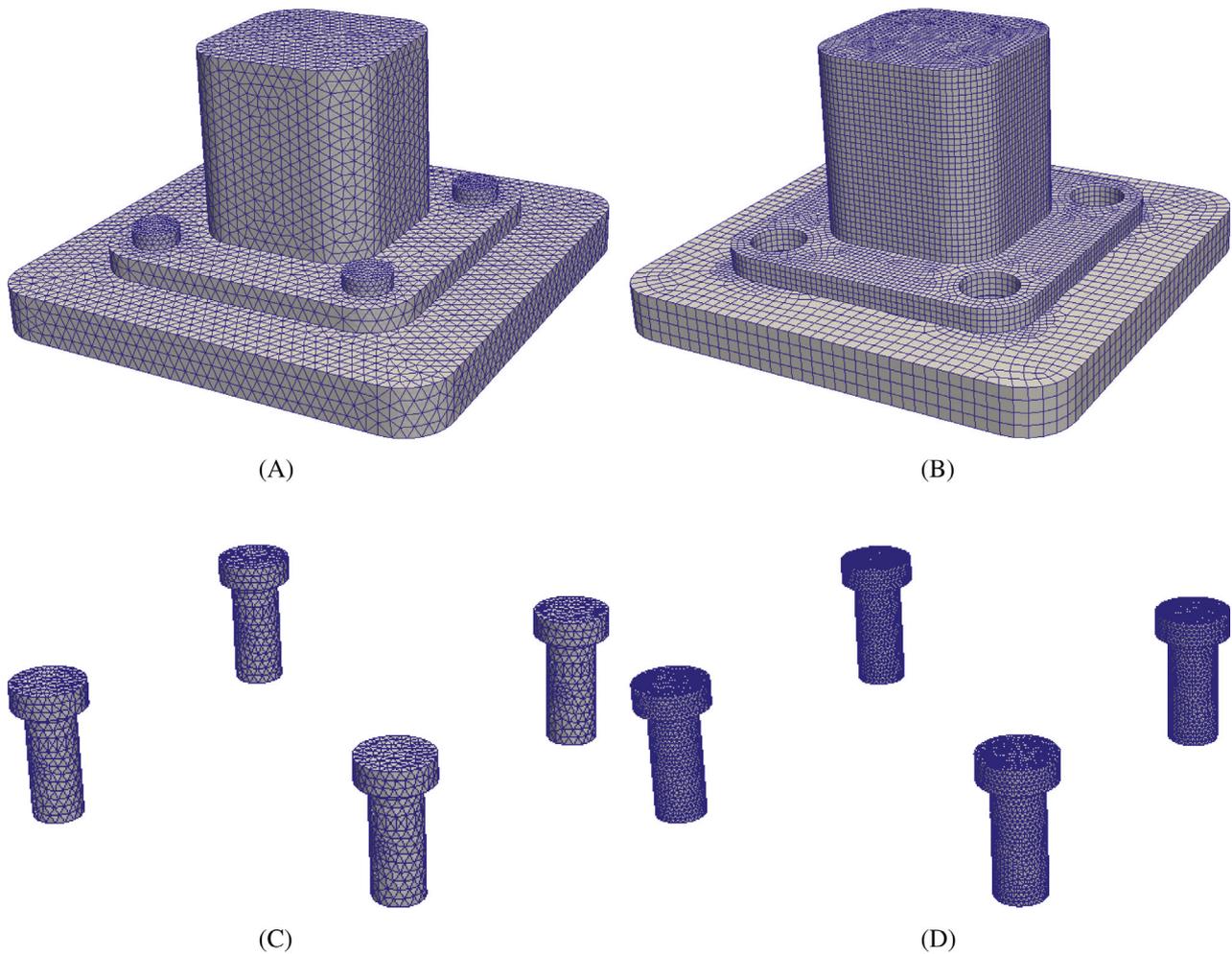
FIGURE 17 Meshes for single domain and Schwarz runs for the bolted joint problem. In the single domain case, we discretize the geometry with a composite tetrahedral mesh (A). For the application of Schwarz, we mesh the parts (Ω_2) with a hexahedral mesh (B), and consider two composite tetrahedral meshes of the bolts: a coarse mesh Ω_1^c (C) and a fine mesh Ω_1^f (D). (A) Composite tetrahedral mesh of single domain (Ω^c); (B) hexahedral mesh of the parts (Ω_2) for Schwarz coupling; (C) coarse composite tetrahedral mesh of the bolts (Ω_1^c) for Schwarz coupling; (D) fine composite tetrahedral mesh of the bolts (Ω_1^f) for Schwarz coupling

TABLE 11 Node and element counts for the single domain and Schwarz meshes considered for the bolted-joint geometry, with the element type in brackets

	Parts		Bolts	
	Elements	**Nodes**	**Elements**	**Nodes**
Single domain (Ω^c)	101,381 [ct-10]	89,534	17,238 [ct-10]	26,667
Schwarz with coarser mesh of bolts Ω_1^c	38,728 [hex]	47,209	15,576 [ct-10]	24,188
Single domain with finer mesh (Ω^f)	162,978 [ct-10]	240,872	132,400 [ct-10]	190,096
Schwarz with finer mesh of bolts Ω_1^f	38,728 [hex]	47,209	132,060 [ct-10]	189,428

Note: The shorthand "ct-10" refers to the composite tetrahedron element.

(A)

(B)

(C)

x-displacement
9.745e-03
0.0073002
0.0048553
0.0024105
-3.439e-05

(D)
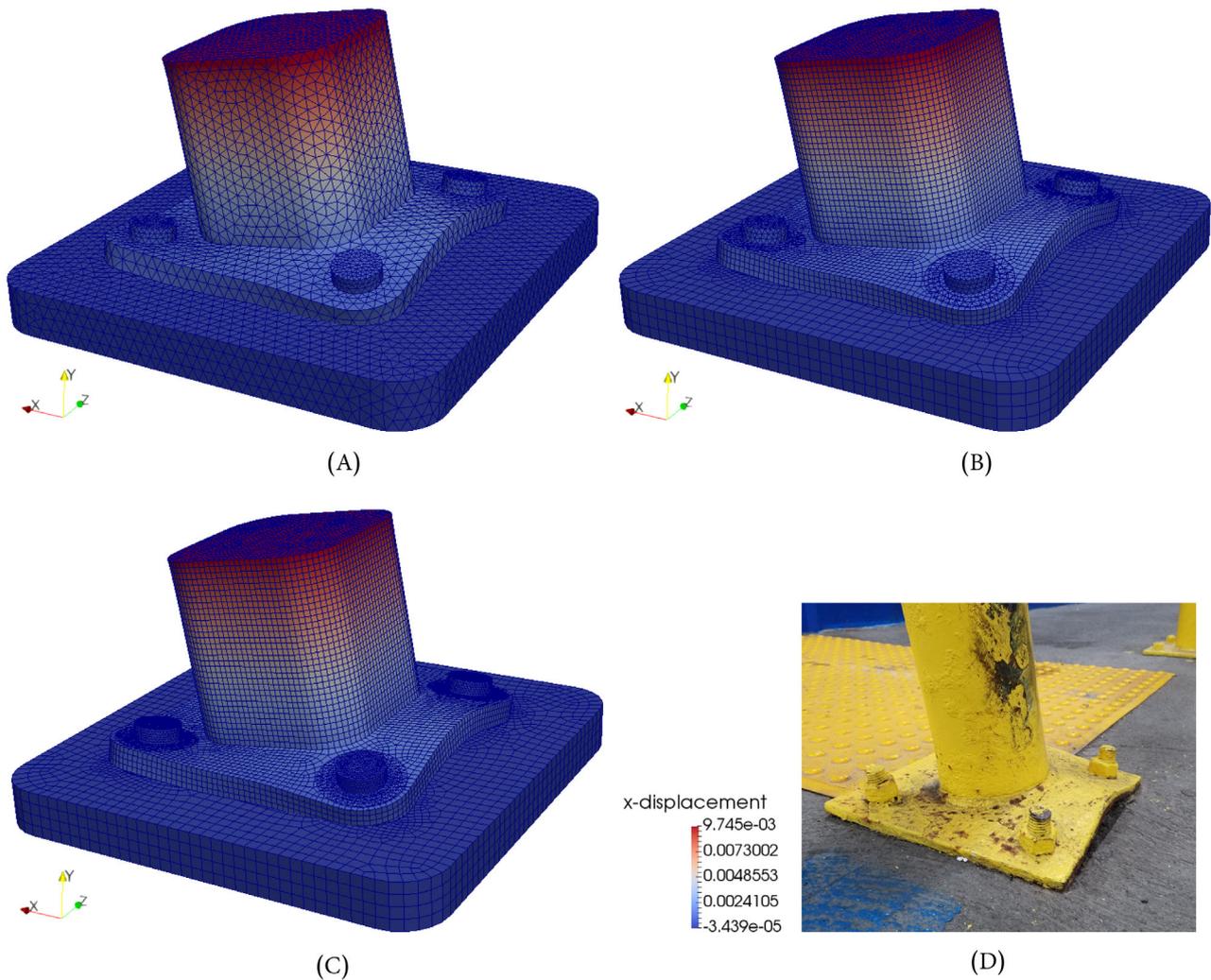
FIGURE 18 The *x*-component of the displacement computed using the traditional finite element method and the proposed dynamic Schwarz coupling at time $t = 4.87 \times 10^{-4}$ s. The time integrator for all runs was implicit Newmark with variable time stepping. The displayed solutions are indistinguishable from one another, and exhibit deformation similar in nature to a real-world reference geometry (D). The 10-node tetrahedral element counts for the bolts subregion for each discretization are as follows: (A) 17,238, (B) 15,576, (C) 132,060. (A) Single domain (Ω^c) solution; (B) Schwarz solution for Ω_1^c and Ω_2; (C) Schwarz solution for Ω_1^f and Ω_2; (D) similarly deformed real joint
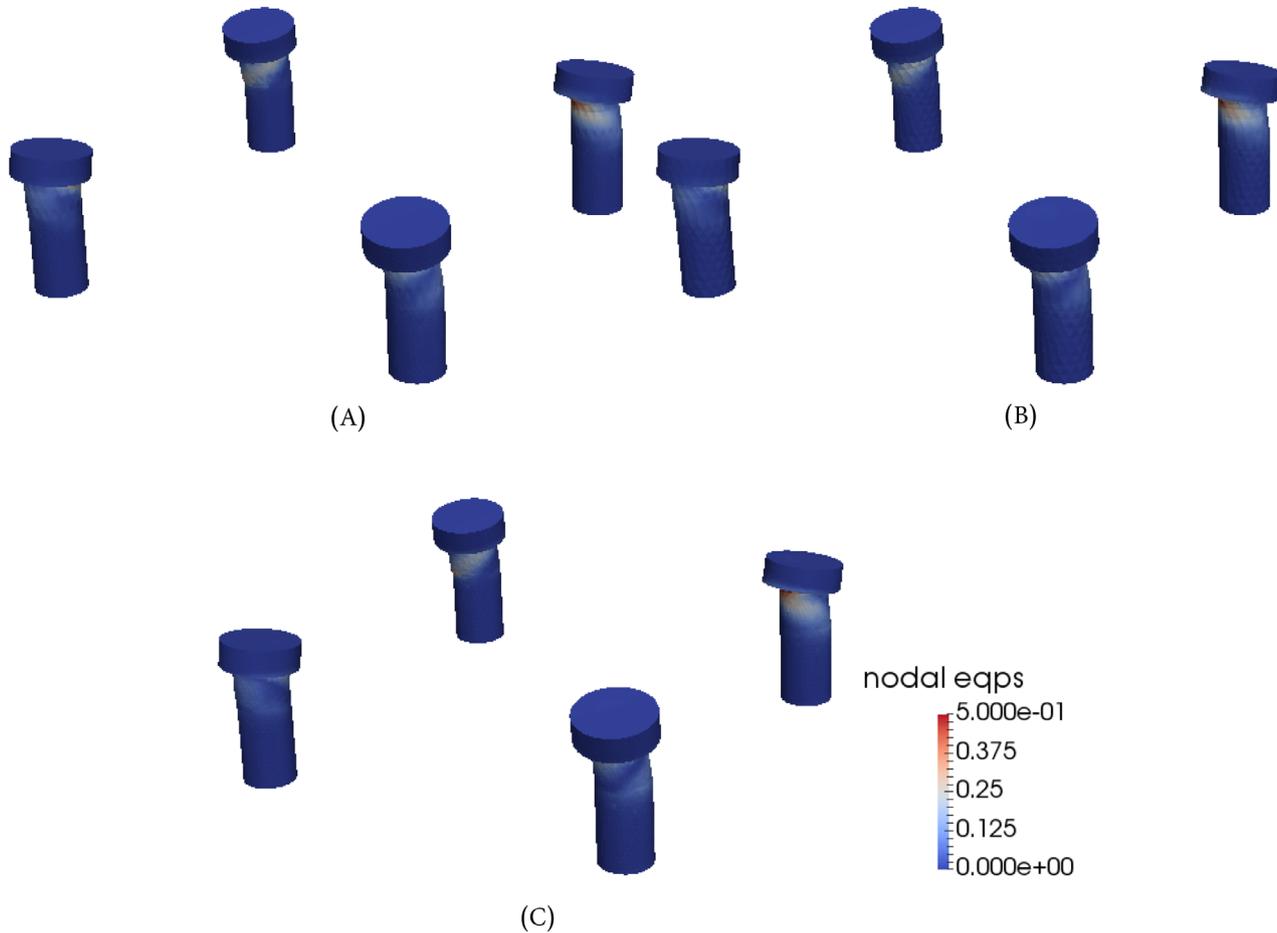
FIGURE 19 Nodal equivalent plastic strain (eqps) in the bolts computed using the traditional finite element method and the proposed dynamic Schwarz coupling at time $t = 4.87 \times 10^{-4}$ s. The time integrator for all runs was implicit Newmark with variable time stepping. The 10-node tetrahedral element counts for the bolts subregion for each discretization are as follows: (A) 17,238, (B) 15,576, (C) 132,060. (A) Single domain (Ω^c) solution for nodal eqps; (B) Nodal eqps solution obtained via Schwarz coupling of Ω_1^c and Ω_2; (C) Nodal eqps solution obtained via Schwarz coupling of Ω_1^f and Ω_2

domain runs use composite tetrahedral meshes of the bolted joint geometry. The first mesh is the previously considered mesh denoted by Ω^c, which contains 118,619 elements. The second mesh is much more refined, and will be denoted Ω^f. This second mesh contains 295,378 elements. The single domain meshes Ω^c and Ω^f contain 17,238 and 132,400 elements within the bolts subregion, respectively. These discretizations are comparable to the Schwarz runs with Ω_1^c and Ω_1^f respectively. For both the Schwarz and the single domain simulations, the time-step control algorithm never had to augment or reduce the time-step, so that a constant time-step $\triangle t = 1.0 \times 10^{-6}$ s was employed in all the simulations considered here. Table 11 summarizes the number of elements and nodes in all the meshes considered here.

The study was performed on a Linux cluster locate at Sandia National Laboratories containing 144 Intel(R) Xeon(R) Gold 6154 3.00 GHz Skylake CPUs, by utilizing 64 of the available CPUs. The reader can observe that the Schwarz simulation with the coarser mesh of the bolts Ω_1^c actually took about 33% *less* time than coarser single domain simulation on Ω^c, which had a comparable number of elements used to represent the bolts. In contrast, the Schwarz simulation with the finer mesh of the bolts Ω_1^f is 74% slower than the single-domain simulation on Ω^f. This situation can likely be ameliorated by specifying a looser Schwarz tolerance than the one employed in these runs (1.0×10^{-6}). We emphasize that the advantage of the Schwarz method here is its "plug-and-play" nature: the method allows one to easily consider different geometries and discretizations for the bolts. Creating conformal meshes of more complex variants of our bolted joint geometry (e.g., if threading is added to the bolts) can be an extremely time-consuming process, in contrast. These two cases for the bolted joint are not enough to draw definite conclusions about the time performance of the Schwarz method,
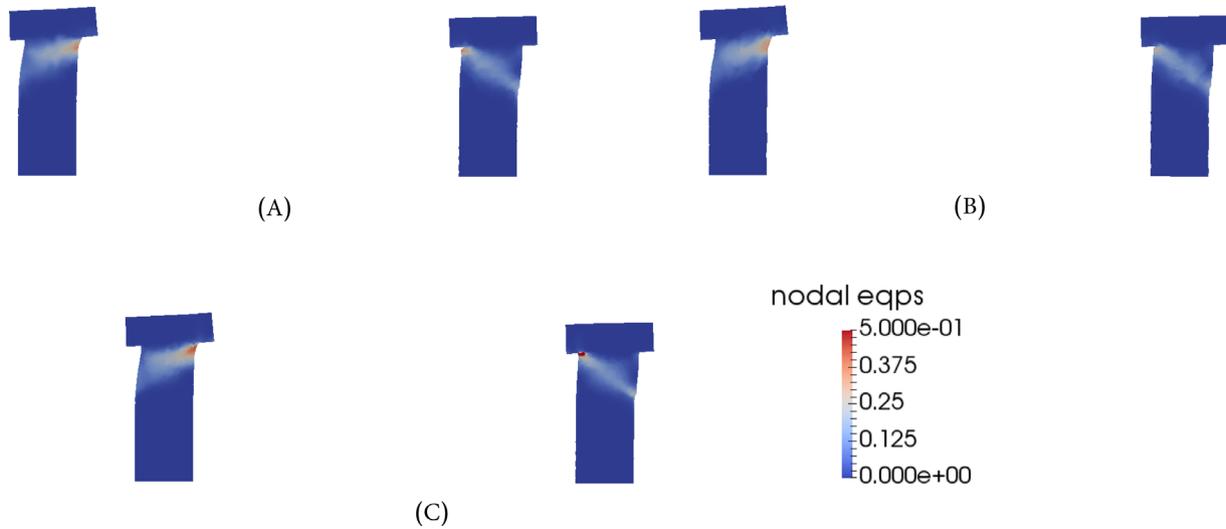
FIGURE 20 Nodal equivalent plastic strain (eqps) in the bolts computed using the traditional finite element method and the proposed dynamic Schwarz coupling at time $t = 4.87 \times 10^{-4}$ s. The time integrator for all runs was implicit Newmark with variable time stepping. Strain concentrations are higher when the bolts are discretized with a finer mesh (C), which is an indication that the coarser mesh is too coarse. The 10-node tetrahedral element counts for the bolts subregion for each discretization are as follows: (A) 17,238, (B) 15,576, (C) 132,060. (A) Single domain (Ω^c) solution for nodal eqps; (B) Nodal eqps solution obtained via Schwarz coupling of Ω_1^c and Ω_2; (C) Nodal eqps solution obtained via Schwarz coupling of Ω_1^f and Ω_2
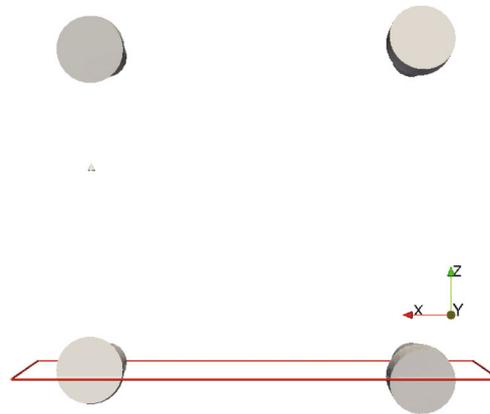
FIGURE 21 Depiction of slice through bolts used to generate Figure 20
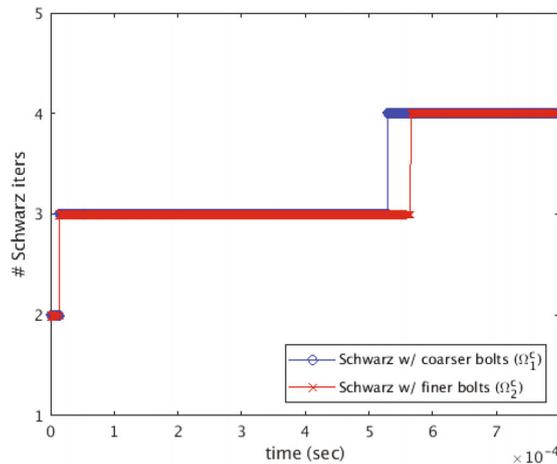
FIGURE 22 Number of Schwarz iterations as a function of time for the bolted joint problem

TABLE 12 Single domain versus Schwarz performance data for the bolted-joint problem (CPU times are averaged over 64 CPUs)

	CPU times	Avg # Schwarz iters	Max # Schwarz iters
Single domain (Ω^c)	3h 34m	-	-
Schwarz with coarser mesh of bolts Ω_1^c	2h 42m	3.32	4
Single domain with finer mesh (Ω^f)	17h 00m	-	-
Schwarz with finer mesh of bolts Ω_1^f	29h 29m	3.28	4

and additional studies in many more situations are needed to determine and tune its performance. We emphasize that even if the method is more expensive computationally for certain mesh resolutions, the alternating Schwarz coupling framework may be preferred for its ability to rapidly change and evaluate a variety of engineering designs, our typical use case.

4 | CONCLUSIONS

Concurrent multiscale methods for solid mechanics are essential for the understanding and prediction of behavior of engineering systems when a small scale event eventually determines the performance of an entire system. The Schwarz alternating method has been adapted and implemented for use in concurrent multiscale coupling. The main advantage of this method is its "plug-and-play" nature, as it enables one to easily consider different geometries and discretizations for different subdomains comprising a targeted engineered component, such as a bolted joint.

In this article, we extended to transient dynamics the Schwarz alternating method proposed in our previous work for quasi-static multiscale analysis.[6] We developed a practical implementation of the method in terms of traditional time stepping schemes, which we showed is equivalent to performing the Schwarz algorithm in space-time. We derived a heuristic criterion on based on the size of the time step to show that the analysis of convergence developed in Mota et al.[6] also applies to the dynamic case. We implemented the proposed dynamic Schwarz algorithm in two codes, ALBANY LCM and SIERRA, and evaluated the method's performance on several numerical examples, including a bolted joint specimen problem of practical interest. We demonstrated by means of these numerical examples that the method does not introduce dynamic artifacts that have been observed with other coupling methods in dynamics. We also showed that the proposed method is capable of coupling conformal meshes, non-conformal meshes, meshes with different levels of refinement, and meshes with different element topologies, as well as different time integrators with different time-steps. Lastly, we illustrated that, despite its iterative nature, the Schwarz alternating method can actually lead to a reduction in CPU time relative to a single-domain simulation that has a comparable resolution.

Future work will focus on several further extensions of the alternating Schwarz methodology, including advancing the method to enable coupling of structural elements to continuum elements, exploring the use of Schwarz-like algorithms for simulating contact, and the development of a multi-physics coupling framework based on variational formulations and the Schwarz alternating method.

DATA AVAILABILITY STATEMENT

The interested user may reproduce the majority of the results presented herein by downloading and installing ALBANY LCM from its public repository on github: https://github.com/sandialabs/LCM. Input files for running the linear elastic wave propagation problem (Section 3.3), the torsion problem (Section 3.4) and the bolted-joint problem (Section 3.5) are available for download here: https://github.com/ikalash/Schwarz-4-Multiscale. These input files have been tested to work with the following versions of TRILINOS (https://github.com/trilinos/Trilinos), ALBANY LCM (https://github.com/sandialabs/LCM) and DTK (https://github.com/ikalash/DataTransferKit):

- TRILINOS: 7bc3b9f7fee156407cdb17b4e59b26f2c3ec9abb,

- ALBANY LCM: fb72244e4c250a720735a2cc08629f9813a9552c,

- DTK: d9a5ccb81f404786a05d40b901c68877a17e356f.

It is noted that a Sandia proprietary code, SIERRA, was used to generate the results in Section 3.5. It is not possible to make this code open-source; however, the same problem can be run in ALBANY LCM, which is open-source. Results presented in Section 3.3.4, in which different time-steps are used in different subdomains for the linear elastic wave propagation problem, can be reproduced by running a MATLAB code that discretizes this problem using the Schwarz alternating method. This code is available for download at the following URL: https://github.com/ikalash/Schwarz-4-Multiscale/tree/main/Dynamic/MATLAB/Schwarz-1D.

ENDNOTES

*ALBANY LCM is available on GitHub: https://github.com/SNLComputation/LCM.

†ALBANY is available on GitHub: https://github.com/SNLComputation/Albany.

‡TRILINOS is available on GitHub: https://github.com/trilinos/trilinos.

§Custom DTK is available on GitHub: https://github.com/ikalash/DataTransferKit (dtk-2.0-tpetra-static-graph branch).

¶The same behavior is observed in an error analysis of a single-domain discretization of the torsion problem with respect to a reference solution computed on a finer mesh.

ORCID

Alejandro Mota https://orcid.org/0000-0003-4268-5397
Irina Tezaur https://orcid.org/0000-0002-0918-5553

REFERENCES

1. Ben DH. Multiscale mechanical problems: the Arlequin method. *Comptes Rendus l'Acad Sci Ser IIB Mech Phys Astron.* 1998;326(12):899-904.

2. Guidault PA, Belytschko T. On the L2 and the H1 couplings for an overlapping domain decomposition method using Lagrange multipliers. *Int J Numer Methods Eng.* 2007;70(3):322-350.

3. Bauman P, Ben Dhia H, Elkhodja N, Oden J, Prudhomme S. On the application of the Arlequin method to the coupling of particle and continuum models. *Comput Mech.* 2008;42:511-530.

4. Prudhomme S, Ben Dhia H, Bauman P, Elkhodja N, Oden J. Computational analysis of modeling error for the coupling of particle and continuum models by the Arlequin method. *Comput Methods Appl Mech Eng.* 2008;197(41-42):3399-3409. Recent advances in computational study of nanostructures.

5. Parks M, Bochev P, Lehoucq R. Connecting atomistic-to-continuum coupling and domain decomposition. *Multiscale Model Simul.* 2008;7(1):362-380.

6. Mota A, Tezaur I, Alleman C. The Schwarz alternating method in solid mechanics. *Comput Methods Appl Mech Eng.* 2017;319:19-51.

7. Belytschko T, Xiao SP. Coupling methods for continuum model with molecular model. *Int J Multiscale Comput Eng.* 2003;1(1):115-126.

8. Schwarz H. Über einen Grenzübergang durch alternierendes Verfahren. *Vierteljahrsschr Naturforschenden Ges Zurich.* 1870;15:272-286.

9. Smith B, Bjorstad P, Gropp W. *Domain Decomposition: Parallel Multilevel Methods for Elliptic Partial Differential Equations.* Cambridge University Press; 1996.

10. Toselle A, Widlund O. Domain decomposition techniques. In: Bruaset AM, Tveito A, eds. *Numerical Solution of Partial Differential Equations on Parallel Computers.* Springer; 2006:135-163.

11. Mathew T. *Domain Decomposition Methods for the Numerical Solution of Partial Differential Equations.* Springer-Verlag; 2008.

12. Quarteroni A. *Numerical Methods for Differential Problems.* Springer; 2009.

13. Gander MJ. Schwarz methods over the course of time. *Electron Trans Numer Anal.* 2008;31:228-255.

14. Hadjiconstantinou N, Patera A. Heterogeneous atomistic-continuum representations for dense fluid systems. *Int J Mod Phys C.* 1997;8(4):967-976.

15. Pandurangan V, Li H, Ng T. A concurrent multiscale method based on the alternating Schwarz scheme for coupling atomic and continuum scaled with first-order compatibility. *Comput Mech*. 2011;47:1-16.

16. Werder T, Walther J, Koumoutsakos P. Hybrid atomistic-continuum method for the simulation of dense fluid flows. *J Comput Phys*. 2005;205:373-390.

17. Anciaux G, Junge T, Hodapp M, Cho J, Molinari JF, Curtin W. The coupled atomistic/discrete-dislocation method in 3D part I: concept and algorithms. *J Mech Phys Solids*. 2018;118:152-171.

18. Hodapp M, Anciaux G, Molinari JF, Curtin W. Coupled atomistic/discrete-dislocation method in 3D part II: validation of the method. *J Mech Phys Solids*. 2018;119:1-19.

19. Cho J, Molinari JF, Curtin WA, Anciaux G. The coupled atomistic/discrete-dislocation method in 3D part III: dynamics of hybrid dislocations. *J Mech Phys Solids*. 2018;118:1-14.

20. Engel M, Griebel M. Flow simulation on moving boundary-fitted grids and application to fluid-structure interaction problems. *Int J Numer Methods Fluids*. 2005;50(4):437-468.

21. Borrel M, Halpern L, Ryan J. Euler/Navier-Stokes couplings for multiscale aeroacoustic problems. Proceedings of the 20th AIAA Computational Fluid Dynamics Conference, Honolulu, Hawaii; 2011.

22. Ryan J, Halpern L, Borrel M. Domain decomposition vs. overset Chimera grid approaches for coupling CFD and CAA. Proceedings of the 7th International Conference on Computational Fluid Dynamics (ICCFD7–1205), Big Island, Hawaii; 2012.

23. Buffoni M, Telib H, Iollo A. Iterative methods for model reduction by domain decomposition. Technical report 6383; INRIA Report; 2007.

24. Cinquegrana D, Viviani A, Donelli R. A hybrid method based on POD and domain decomposition to compute the 2-D aerodynamic flow field - incompressible validation. Proceedings of the AIMETA 2011- XX Congresso dell'Associazione Italiana di Meccanica Teorica e Applicata, Bologna, ITA; 2011.

25. Maier I, Haasdonk B. A Dirichlet-Neumann reduced basis method for homogeneous domain decomposition problems. *Appl Numer Math*. 2014;78:31-48.

26. Li K, Tang K, Wu T, Liao Q. D3M: a deep domain decomposition method for partial differential equations. *IEEE Access*. 2020;8:5283-5294.

27. Li W, Xiang X, Xu Y. Deep domain decomposition method: elliptic problems. Proceedings of the First Mathematical and Scientific Machine Learning Conference; 2020; Princeton University, Princeton, NJ.

28. Belgacem FB. The Mortar finite element method with Lagrange multipliers. *Numer Math*. 1999;84(2):173-197.

29. Duval M, Passieux JC, Salauen M, Guinard S. Non-intrusive coupling: recent advances and scalable nonlinear domain decomposition. *Arch Comput Methods Eng*. 2016;23(1):17-38.

30. Bettinotti O, Allix O, Perego U, Oancea V, Malherbe B. Simulation of delamination under impact using a global local method in explicit dynamics. *Finite Elements Anal Des*. 2017;125:1-13.

31. Hodapp M. Analysis of a Sinclair-type domain decomposition solver for atomistic/continuum coupling. *Multiscale Model Simul*. 2021;19(4):1499-1537.

32. Gander M, Halpern L, Nataf F. Optimal convergence for overlapping and non-overlapping Schwarz waveform relaxation. In: Lai C-H, Bjorstad PE, Cross M, Widlund OB, eds. *11th International Conference on Domain Decomposition in Science and Engineering*. Domain Decomposition Press; 1999:253-260.

33. Sobolev S. Schwarz's algorithm in elasticity theory. In: Demidenko G, Vaskevich V, eds. *Selected Works of S.L. Sobolev. Volume I: Equations of Mathematical Physics, Computational Mathematics and Cubature Formulas*. Springer; 2006.

34. Mikhlin S. On the Schwarz algorithm. *Proc USSR Acad Sci (in Russian)*. 1951;77:569-571.

35. Prager M. Schwarzuv algoritmus pro polyharmonické funkce. *Apl Mat*. 1958;3(2):106-114.

36. Morgenstern D. Bedründung des alternierenden Verfahrens durch orthogonalprojektion. *ZAMM*. 1956;36:7-8.

37. Babuška I. On the Schwarz algorithm in the theory of differential equations of mathematical physics (in Russian). *Chechoslovak Math J*. 1958;8(3):328-343.

38. Lions P. On the Schwarz alternating method I. Proceedings of the First International Symposium on Domain Decomposition methods for Partial Differential Equations, 1988; SIAM, Philadelphia.

39. Badea L. On the Schwarz alternating method with more than two subdomains for nonlinear monotone problems. *SIAM J Numer Anal*. 1991;28(1):179-204.

40. Lui S. On linear monotone iteration and Schwarz methods for nonlinear elliptic PDEs. *Numer Math*. 2002;93:109-129.

41. Mota A, Tezaur I, Hoy J. The Schwarz alternating method for multiscale contact mechanics. *Math Comput Appl*. 2022; (in preparation).

42. Boglaev I, Sirotkin VV, Lavers J. The computation of transient 2-D eddy current problem by domain decomposition algorithms. *Math Comput Model*. 1995;21:39-51.

43. Marsden J, Ratiu TS *Introduction to Mechanics and Symmetry: A Basic Exposition of Classical Mechanical Systems*. Springer-Verlag; 1999.

44. Heroux M, Bartlett R, Howle V, et al. An overview of Trilinos. Technical report SAND2003-2927; Sandia National Laboratories Report; 2003.

45. Spotz W, Smith T, Demeshko I, Fike J. Aeras: a next generation global atmosphere model. *Proc Comput Sci*. 2015;51:2097-2106.

46. Tezaur I, Perego M, Salinger A, Tuminaro R, Price S. Albany/FELIX: a parallel, scalable and robust finite element higher-order stokes ice sheet solver built for advanced analysis. *Geosci Model Dev*. 2015;8:1197-1220.

47. Gao X, Nielsen E, Muller R, et al. Quantum computer aided design simulation and optimization of semiconductor quantum dots. *J Appl Phys*. 2013;114:1-19.

48. Sun W, Ostien J, Salinger A. A stabilized assumed deformation gradient finite element formulation for strongly coupled poromechanical simulations at finite strain. *Int J Numer Anal Methods Geomech*. 2013;37:2755-2788.

49. Salinger A, Bartlett R, Bradley A, et al. Albany: using agile components to develop a flexible, generic multiphysics analysis code. *Int J Multiscale Comput Eng*. 2016;14:415-438.

50. Slattery S, Wilson P, Pawlowski R. The Data Transfer Kit: a geometric rendezvous-based tool for multiphysics data transfer. Proceedings of the International Conference on Mathematics and Computational Methods Applied to Nuclear Science and Engineering; 2013; American Nuclear Society, Sun Valley, ID.

51. Ober C, Conde S, Pawlowski R. Tempus: time integration package; 2018. https://trilinos.github.io/tempus.html

52. SIERRA Solid Mechanics Team. Sierra/solid mechanics 4.48 user's guide. Technical report SAND-2018-2961, Sandia National Laboratories Report; 2018.

53. Farhat C, Lesoinne M, LeTallec P, Pierson K, Rixen D. FETI-DP: a dual-primal unified FETI method—part I: a faster alternative to the two-level FETI method. *Int J Numer Methods Eng*. 2001;50(7):1523-1544.

54. Ostien J, Foulk J, Mota A, Veilleux M. A 10-node composite tetrahedral finite element for solid mechanics. *Int J Numer Methods Eng*. 2016;107:1145-1170.

55. Newmark N. A method of computation for structural dynamics. *J Eng Mech, ASCE*. 1959;85(3):67-94.

56. Mota A, Chen Q, Foulk JW, Ostien JT, Lai Z. A Cartesian parametrization for the numerical analysis of material instability. *Int J Numer Methods Eng*. 2016;108(2):156-180.

57. Kane C, Marsden J, Ortiz M, West M. Variational integrators and the Newmark algorithm for conservative and dissipative mechanical systems. *Int J Numer Methods Eng*. 2000;49(10):1295-1325.

APPENDIX A. CONVERGENCE OF THE SCHWARZ ALTERNATING METHOD FOR TRANSIENT SOLID DYNAMICS

In this section, we provide some conditions under which the Schwarz method for solid dynamics described in Section 2.2 converges. In essence, we rely on the analysis of the Schwarz alternating method performed by Lions, who defines the conditions for convergence for monotone nonlinear problems. Provided that the time step is small enough, the discrete problem at each time step reduces to an elliptic problem whose tangent matrix is diagonally dominant, and for which the analysis in Section I.5 of Lions[38] applies, proving linear convergence of the method.

To determine if the problem defined by (8)–(10) is well posed, and therefore whether the Schwarz coupling method will converge to the solution, we investigate the second variation of the action functional (4) given by

$$\delta^2 S := D^2 S[\boldsymbol{\varphi}](\boldsymbol{\xi}, \boldsymbol{\xi}) = \int_I \int_\Omega \Lambda(\boldsymbol{X}, t) \, dV dt,$$

$$\Lambda(\boldsymbol{X}, t) := \rho_0 \dot{\boldsymbol{\xi}} \cdot \dot{\boldsymbol{\xi}} - \text{Grad } \boldsymbol{\xi} : \mathbb{A} : \text{Grad } \boldsymbol{\xi}, \tag{A1}$$

where $\mathbb{A} := \partial^2 A / \partial \boldsymbol{F} \partial \boldsymbol{F}$ is the fourth-order tensor of tangent moduli. The action functional $S[\boldsymbol{\varphi}]$ in (4) is strictly convex if $\Lambda(\boldsymbol{X}, t) > 0$ for all $(\boldsymbol{X}, t) \in \Omega \times I$, and strictly concave if $\Lambda(\boldsymbol{X}, t) < 0$ for all $(\boldsymbol{X}, t) \in \Omega \times I$, respectively; otherwise this test is indeterminate. For the strictly convex and strictly concave cases, the arguments advanced in Lions[38] for the convergence of the Schwarz alternating method apply directly here. In other words, the Schwarz alternating method converges provided that the problem defined by $S[\boldsymbol{\varphi}]$ is well-posed, that is, it has a solution and that solution is unique. Next, we examine the conditions that are required for the strictly convex and strictly concave cases.

The first term in $\Lambda(\boldsymbol{X}, t)$ is $\rho_0 \dot{\boldsymbol{\xi}} \cdot \dot{\boldsymbol{\xi}}$. This is guaranteed to be always greater or equal to zero for all $(\boldsymbol{X}, t) \in \Omega \times I$, since the mass density $\rho_0 > 0$. If it is equal to zero, the action functional is concave and the problem is quasi-static. For this case, and provided the following strong-ellipticity condition holds, the relevant convergence analysis is given in Lions.[38]

The second term in $\Lambda(\boldsymbol{X}, t)$ is $\text{Grad } \boldsymbol{\xi} : \mathbb{A} : \text{Grad } \boldsymbol{\xi}$. This admits an interpretation as the *strong ellipticity condition* for finite-deformation solid mechanics.[56] The strong ellipticity condition can be expressed as

$$(\boldsymbol{m} \otimes \boldsymbol{n}) : \mathbb{A} : (\boldsymbol{m} \otimes \boldsymbol{n}) > 0, \quad \forall \, \boldsymbol{m}, \boldsymbol{n} \in \mathbb{R}^3. \tag{A2}$$

The loss of the strong ellipticity condition is associated with the presence of material instabilities, and plays an important role in the simulation of material failure. The analysis of numerical instability under material failure is beyond the scope

of this work, and the reader is referred to works on numerical techniques for material failure.[56] Nevertheless, for localized failure under the control of regularization, the heuristic method discussed below applies.

The indeterminate case, where $\delta^2 S$ is neither strictly convex or strictly concave, is perhaps the most common. Without additional information, however, nothing concrete can be said about the nature of the action functional, until the introduction of discretizations for both space and time. We address this in a heuristic fashion below.

For concreteness and to fix ideas, let us introduce a standard finite element discretization into the action functional (4), thereby obtaining a discrete variational statement corresponding to (7). Let us introduce also a standard time integrator such as Newmark, and then linearize to use a Newton-type scheme to solve the attendant nonlinear system of equations. This is lengthy, but straightforward, and the end result for the discretized version of (A1) is

$$\delta^2 S[\varphi_h] := \boldsymbol{x}^{\mathrm{T}} \left[\frac{\gamma^2}{(\beta \, \triangle t)^2} \boldsymbol{M} + \boldsymbol{K} \right] \boldsymbol{x}, \tag{A3}$$

where $\boldsymbol{M}$ is the mass matrix, $\boldsymbol{K}$ is the stiffness matrix, $\triangle t$ is the time step, and β and γ are the parameters for the Newmark method, usually set to $\frac{1}{4}$ and $\frac{1}{2}$.[57] For well-defined problems, $\boldsymbol{M}$ is always symmetric and positive definite, while $\boldsymbol{K}$ may also be assumed to be symmetric and positive definite. In that case, it becomes clear that for non-trivial solutions, (A3) can always be made positive by choosing an appropriately small time step $\triangle t$. The size of that time step depends on the properties of both the mass and stiffness matrices. In our simulations, the size of the time step was dictated by other considerations, such as stability for explicit time integration, or the need to have a sufficiently small time step to be able to solve the attendant nonlinear system associated with large-deformation plasticity.

In conclusion, the second variation of the dynamical problem represented by the action functional (4) can be rendered positive by choosing a sufficiently small time step once it is discretized both in space and time. This in turn allows the use of the analysis presented by Lions for nonlinear monotone problems.[38] We show the application of the Schwarz method to dynamic problems in the preceding sections, where the size of time step was dictated in every instance by other considerations rather than the criterion discussed above, since this appears to be a rather conservative estimate. For instance, for the elastic wave propagation problem of Section 3.3, this estimate yields a value of $\triangle t < 10^{-6}$ s to guarantee that (A3) will be positive. However, in order to resolve the propagation of the waves, we choose time steps one order the magnitude smaller, $\triangle t \approx 10^{-7}$ s.

Finally, it is noted that, like for the quasistatic case, convergence of our dynamic Schwarz alternating formulation is requisite on performing the domain decomposition such that the overlap region(s) is (are) non-empty; for details, the reader is referred to Lions.[38] In general, faster convergence of the Schwarz method is observed for larger overlap regions, as shown numerically in Section 3.